Title

Understanding asymmetric switching times in accumulation mode organic electrochemical transistors

Author list

Jiajie Guo,[1†] Shinya E. Chen,[1†] Rajiv Giridharagopal,[2] Connor G. Bischak,[2] Jonathan W. Onorato,[3] Kangrong Yan,[4] Ziqiu Shen,[4] Chang-Zhi Li,[4] Christine K. Luscombe,[3,5] David S. Ginger[2].*

Affiliations

[1] Molecular Engineering and Sciences Institute, University of Washington, Seattle, WA 98195, United States.
[2] Department of Chemistry, University of Washington, Seattle, WA 98195, United States.
[3] Department of Materials Science and Engineering, University of Washington, Seattle, WA 98195, United States.
[4] State Key Laboratory of Silicon and Advanced Semiconductor Materials, Department of Polymer Science and Engineering, Zhejiang University, Hangzhou 310027, P.R. China.
[5] pi-Conjugated Polymers Unit, Okinawa Institute of Science and Technology Graduate University, Onna-son, Okinawa, 904-0495, Japan.

[†] These two authors contributed equally to the work.
* Corresponding author e-mail, dginger@uw.edu

Abstract

Understanding the factors underpinning device switching times is crucial for the implementation of organic electrochemical transistors (OECTs) in neuromorphic computing, bioelectronics, and real-time sensing applications. Existing models of device operation cannot explain the experimental observations that turn-off times are generally much faster than turn-on times in accumulation mode OECTs. Using operando optical microscopy, we image the local doping level of the transistor channel and show that turn-on occurs in two stages, propagation of a doping front, followed by uniform doping, while turn-off occurs in one stage. We attribute the faster turn-off to a combination of engineering as well as physical and chemical factors including channel geometry, differences in doping and dedoping kinetics, and the phenomena of carrier density-dependent mobility. We show that ion transport limits the operation speed in our devices. Our study provides insights into the kinetics of OECTs and guidelines for engineering faster OECTs.

Main text

Organic electrochemical transistors (OECTs) are currently being explored for applications including bioelectronics,[1–4] logic circuit elements,[5,6] and neuromorphic devices.[7–12] As a class of transistors, OECTs feature high transconductance (≈ mS),[13] low operation voltage (typically < |1 V|),[13] and direct response to biologically relevant ions[14,15] and neurotransmitters.[16,17] The relatively soft nature of organic semiconductors used in OECTs enables the detection of action potentials[2,18] in mechanically flexible environments and enables applications in brain-machine interfaces and in vivo sensing.[19–21] To unleash the full potential of OECTs, a deeper understanding of the fundamental transistor operation mechanisms is necessary, especially transistor switching behaviors, which are critical to the training phase of neuromorphic computing and to both simulating behaviors of arrays of transistors and their scaling properties.[22,23]

In OECTs, organic mixed ionic-electronic (semi)conductors (OMIECs) are used as channel active layers, with the most common materials being conjugated polymers.[24–28] The conductivity of an OECT is modulated by the electrochemical gate potential, which controls the doping level (redox state) of the conjugated polymer channel. Importantly, in contrast to conventional field-effect transistors (FETs), OECTs exhibit volumetric doping: the gate voltage changes the conductivity of the entire volume of the transistor channel, rather than just the surface layer, and counterions injected from the electrolyte provide charge compensation for injected electronic carriers.[29] At steady-state, the channel current (I_D) is governed by both carrier mobility and carrier density. The steady-state behavior of OECTs has been relatively well studied.[24,25,30,31] To benchmark the device performance, the product of electronic mobility and volumetric capacitance, μC^*, is recognized in the literature as the material figure of merit of OECT in steady-state operation.[32]

Compared to the steady-state performance, our current knowledge of OECT kinetics is limited.[31] For example, the switching speed for materials with identical μC^* can vary by many orders of magnitude.[33]

Understanding the switching behaviors of OECTs is crucial for designing logic units as well as emulating and sensing neural activity, which typically operates at the frequency of ≈ 100 Hz.[18] The widely-used Bernards model describes the transient behavior with an equivalent RC circuit as the ionic path and makes the quasistatic approximation for the channel charge distribution.[30] Several improved models based on the original Bernards model have been proposed with more complex equivalent circuits describing the ionic circuit.[34,35] Recently, Paudel *et al.* demonstrated a 2D-finite element model that shows the existence of the lateral ion current during switching.[36] These kinetics studies are all based on poly(3,4-ethylenedioxythiophene):poly(styrene sulfonate) (PEDOT:PSS), which operates as a depletion mode OECT, and may not be directly comparable to accumulation mode OECTs. To our best of knowledge, only one recent study by Keene et al. has started to discuss the transient response of accumulation mode OECTs, focusing on device turn-on kinetics.[37]

Asymmetric OECT response times

Figure 1a shows a typical transient response of an accumulation mode OECT: the transistor is turned on (higher $|I_D|$) upon gate potential applied and is turned off upon potential removal. We first use the Bernards model[30] to describe the transistor switching behavior (**Supplementary Note 1**). The Bernards model expresses the variation of I_D over time as a single exponential function following a square V_G pulse, with one RC time constant related to ion transport into the channel polymer.[30] We find that the Bernards model fails to predict three aspects of the transient response for accumulation mode OECTs: (1) the initial transistor turn-on, which shows a short delay in experiments (**Fig. 1a**, bottom left) rather than instant turn-on; (2) the experimental transistor turn-on is not a single exponential function; (3) the difference in transistor switching-on and switching-off times is asymmetric in experiment, but symmetric in the model (**Fig. 1a**). These issues, especially the difference in transistor switching times, cannot be resolved even we apply later models, as these models focus on either incorporating more passive circuit elements into the equivalent circuit or interpreting the pre-exponential factor.[34,35] **Figure 1b** and **Supplementary Table 1** display the turn-on and turn-off times of accumulation mode OECTs from both this paper and our literature survey. **Figure 1b** shows that faster device turn-off compared to turn-on is indeed ubiquitous, though less discussed.[38]

One hypothesis is that this asymmetry could arise from the switching potentials chosen. Based on the Butler–Volmer model, the electrochemical reaction rate is influenced by the activation potential.[39–41] It is possible that the faster turn-off is the result of smaller voltage differences between V_{on} and V_T compared to V_{off} and V_T, namely, $|V_{on} - V_T| < |V_{off} - V_T|$. To rule out the influence of the mismatch between switching on and off gate potentials, we selected three p-type polymers as examples and tested their OECT kinetics with fixed voltage differences between V_T and switching potentials: poly[2,5-bis-(thiophenyl)-1,4-bis(2-(2-(2-methoxyethoxy)ethoxy)ethoxy)-benzene] (PB2T-TEG),[42] poly(3-{[2-(2-methoxyethoxy)ethoxy]methyl}-thiophene-2,5-diyl) (P3MEEMT),[43,44] and poly(3-hexylthiophene-2,5-diyl) (P3HT) (structure and performance in **Supplementary Fig. 1**); and using two aqueous electrolytes:

potassium chloride (KCl) and potassium trifluoromethanesulfonimide (KTFSI). After accounting for threshold voltage, we still observe faster turn-off behavior (**Fig. 1b**, stars). Clearly, the asymmetry in switching times must be related to other factors like polymer doping/dedoping kinetics or device geometry.

Comparison between OECT and spectroelectrochemistry

Because the magnitude of I_D is closely related to the electrochemical doping level of the channel conjugated polymer,[45,46] it is possible that faster OECT turn-off is an inherent consequence of differences in electrochemical doping and dedoping due to, for example, polymer structural changes. We therefore compared the doping and dedoping kinetics of spectroelectrochemistry (two-terminal diodes) to the turn-on and turn-off speed of OECTs (three-terminal transistors). **Figure 2a,b** display the geometries of the spectroelectrochemistry and OECT measurements. **Figure 2c** shows the steady-state UV-Vis spectra, which provides information on the electronic states of the conjugated polymers. When electrochemically doped, the polymer is oxidized by formation of polarons, resulting in the bleaching of the π-π^* transition peak ($\approx$ 525 nm) and increased absorption of the polaron peak ($\approx$ 680 nm). **Figure 2d** shows the drain current vs. drain voltage curves at two different gate voltages corresponding to the on-state (doped) and the off-state (neutral). Time-resolved UV-Vis spectra show the rate of polaron injection and removal, expressed via the time constants: τ_{doping} and $\tau_{dedoping}$. We obtain the time constants by exponential fits of the polaron absorption peak over time (**Fig. 2e** and **Supplementary Figs. 2** and **3**). These kinetics are stable over multiple cycles over the timescales of our experiments (**Supplementary Fig. 4**), indicating no significant sample property changes (i.e., material degradation) during testing. The turn-on and turn-off periods we use (10 s) are sufficiently long ($> 3\tau$) such that any impact from memory of previous cycles is negligible. Below, we refer to similar time constants from the transient response of OECT switching as τ_{on} and τ_{off} to distinguish them from the spectroelectrochemistry time constants (**Fig. 2f** and **Supplementary Figs. 2** and **3**). Given the effect of the activation potential previously discussed, we measured the operando UV-Vis spectra under the same potential difference with respect to the equilibrium potential, or open circuit potential (OCP). The V_T and OCP values are listed in **Supplementary Table 2**.

Figure 2g,h summarize the ratios of $\tau_{doping}/\tau_{dedoping}$ (spectroelectrochemistry) and τ_{on}/τ_{off} (OECT) of four polymer-electrolyte pairs, respectively. We showed that, in both spectroelectrochemistry and OECTs, the processes involving polymer doping are slower than the ones associated with polymer dedoping. However,

across all polymers and electrolytes, the switching difference between these two processes is much larger in OECTs compared to spectroelectrochemistry (**Supplementary Table 3).** Interestingly, we find that the timescale of OECT turn-on is comparable to the timescale for spectroelectrochemical doping, while OECT turn-off is much faster than spectroelectrochemical dedoping (approximately 10-100x faster). These results suggest that faster OECT turn-off is not simply due to faster polymer dedoping.

Operando microscopy characterization

To further understand the origin of faster device turn-off in accumulation mode OECTs, we probe the electrochemical doping level of the conjugated polymer channel via operando optical microscopy coupled with a 650 nm long pass filter to selectively monitor polaron formation (**Fig. 3a**). Even though we cannot probe the ion distribution in the OECT channel directly, Jackson et al. demonstrated good nanometer-scale spatial correlation between counterion and polaron in the doped conjugated polymer film,[47] suggesting the polaron and the counterion densities are correlated, as expected from charge balance. **Figure 3b** shows the transient response of I_D and I_G during transistor turn-on, with the V_D applied and kept constant before applying V_G. This process simulates the case of transistor operation where the V_G is switching the source-drain channel on and off. We observed an immediate I_G response to the V_{on}, which shows a typical spiking and decay behavior, suggesting ion injection from the electrolyte into the channel polymer. In contrast, I_D remains relatively low initially after V_{on} applied, which to our knowledge, has not been discussed previously. **Figure 3c** shows the microscope movie frames during turn-on. Darker pixels represent more polaron absorption and thus a higher electrochemical doping level. We observe that OECT device turn-on occurs in two stages: (1) a *doping front propagation* stage and (2) a *vertical doping* stage.

During the *doping front propagation* stage, we find that even though substantial doping of the channel polymer is already occurring, the growth of the I_D starts only after the doping front position (x_{front}) reaches the drain electrode (**Fig. 3d,e** and **Supplementary Video 1**). We thus introduce the doping front propagation time, t_p, as the time required for the doping front to propagate across the entire channel from the source to the drain electrode, with the value of ≈ 270 ms for this particular device (L = 600 μm). We defined x_{front} as the position of the peak of the first derivative of the absorbance. **Figure 3e** shows the relatively linear relation between x_{front} and time: the front is moving at a constant speed ≈ 2.2 μm/ms in this case. The fact that we observe the doping front propagating from the source to drain electrode suggests that the injection of electronic carriers is occurring primarily from the source electrode during device turn-on, especially in the case where $|V_D| \geq |V_G - V_T|$ (when V_D equals to −0.2 V to -0.6 V). In the case of low V_D

(when V_D equals to −0.1 V), the electronic carrier injection could occur at both source and drain electrodes (**Supplementary Video 2 and Supplementary Fig. 5**), which is in agreement with the phenomenon recently reported.[37] In addition, we note that this doping front propagation stage (I_D remains relatively low after V_{on} applied) may be overlooked if transient response is characterized without high sampling rates.

In the *vertical doping* stage, we observed a similar speed of doping of the polymer in the center of the channel and near both electrodes (**Fig. 3f,g**). We found the time of I_D increase ($\tau_{OECT} \approx 290$ ms) and polymer doping ($\tau_{SpecE} \approx 200$ ms) is at the same order of magnitude, suggesting the I_D increase is largely dominated by the increase of doping level (or carrier density) along the channel with the underlying polymer acting as an increasingly conductive, planar electrode. **Figure 3** shows data from PB2T-TEG, a polymer that undergoes a distinct structural phase transition upon doping.[42] We find this two-stage behavior of a doping front propagating followed by more uniform doping is a general accumulation mode OECT behavior regardless of cycle number (**Supplementary Video 3**), active layer polymer (**Supplementary Video 4**), channel length (**Supplementary Fig. 6**) or in the case where V_D and V_G are applied at the same time during the beginning of transistor turn-on (**Supplementary Video 5)**.

For the OECT device turn-off, or the *vertical dedoping* stage, we observed an immediate response of both I_D and I_G to the V_{off} (**Fig. 3h** and **Supplementary Video 6**). We did not observe a front propagation event compared to turn-on. **Figure 3i,j** displays the polymer dedoping process along the channel. The polymer dedopes relatively uniformly, with faster dedoping very near the source electrode (**Fig. 3k**). This finding partly explains the faster OECT turn-off. If we consider conduction in the transistor channel as through a series of resistors, if the resistance of one of the resistors increases (the polymer near source electrode), the total resistance will increase and thus reduce I_D. Nevertheless, this explanation must be incomplete, as the turn-off speed of I_D is *still* much faster than the dedoping speed of polymer near source electrode. Additionally, we found that even though the transistor is in the off-state already, dedoping of the channel polymer is not fully complete, as noted by the absorbance in the polaron band (**Fig. 3k**). This phenomenon suggests that, through shortening the off-interval (increased duty cycle), faster OECT turn-on

in the subsequent cycle is achievable, as the channel is already in a slightly doped state (**Supplementary Note 2**). We next considered whether carrier-density dependent mobility can account for the remaining operational asymmetry.

Carrier density-dependent mobility

Figure 4a shows the transient response of the I_D, carrier density, and average carrier mobility during the transistor turn-off. We calculated the carrier density using both the integral of gate current over time and average polaron absorbance along the channel during the vertical dedoping stage and both results are in good agreement (**Supplementary Fig. 7**). We then estimated the average hole mobility in the channel via:

$$\mu = \left(\frac{L}{W \cdot d \cdot e \cdot V_D}\right) \cdot \frac{I_D}{p} \quad (1)$$

assuming a linear electric field along the channel, where μ is the average carrier mobility, p is the hole density, e is the electron charge and V_D is the drain voltage. L, W, and d represent channel length, width, and thickness, respectively. We find the turn-off rate of I_D is comparable to the rate of the carrier mobility decay, which, due to the non-linear relationship between density and mobility in conjugated polymers, is about one order of magnitude faster than the carrier removal rate.

Figure 4b shows the calculated carrier mobility as a function of carrier density measured. We find that the carrier mobility is indeed carrier density-dependent, especially in the high carrier density region. Previously, Friedlein et al. demonstrated that the steady-state OECT performance can be well characterized using a carrier density-dependent mobility of the form:

$$\mu = \mu_0 \cdot \left(\frac{p}{p_0}\right)^{\frac{E_0}{k_B T}-1} \quad (2)$$

where μ_0 is mobility prefactor and p_0 is zero-field hole concentration. E_0 describes the energetic width of the tail of the density of states, k_B is Boltzmann's constant and T is temperature.[48] This equation captures the filling of the density of states (DOS) due to energetic disorder in conjugated polymer materials.[49] This relation also fits our extracted carrier mobility versus density data well. **Supplementary Note 3** describes detailed fittings and discussions of Eqn 2. **Supplementary Note 4** shows the impact of E_0 on the asymmetry of OECT turn-on and turn-off time based on the model incorporating Eqn 2. Specifically, we show that the asymmetry increases (larger difference between turn-on and turn-off times) with larger E_0 values (broader

DOS/more amorphous) compared to smaller E_0 values (narrower DOS/more crystalline). This simulated result qualitatively agrees with our experimental results: more crystalline P3HT polymer, with $E_0 \approx 60$ meV,[50] does show smaller difference between $\tau_{doping}/\tau_{dedoping}$ (1.2) and τ_{on}/τ_{off} (5.1) compared to PB2T-TEG, which has $\tau_{doping}/\tau_{dedoping}$ and τ_{on}/τ_{off} values to be 5.8 and 529, respectively. We hypothesize the OECT turn-on/turn-off asymmetry originates partly from the spatially heterogeneous doping and dedoping, and partly from the asymmetric polymer doping/dedoping rate (or the asymmetric carrier injection/ejection rate). This asymmetry is further amplified by the non-linear, density-dependent carrier mobility (Eqn 2), thus explaining the data in **Fig. 2**, showing why transistor behavior is more asymmetric than doping/dedoping kinetics alone would imply.

Engineering faster OECTs

With the knowledge from the operando microscopy, we express the two-stage turn-on with an empirical biexponential equation including the initial front propagation time (t_p):

$$\left|I_{\mathrm{D,\,Norm}}(t)\right| = A_1 \cdot \left(1 - e^{-\frac{t-t_p}{\tau_{1,on}}}\right) + A_2 \cdot \left(1 - e^{-\frac{t-t_p}{\tau_{2,on}}}\right);\ A_1 + A_2 = 1 \quad (3)$$

where $\tau_{1,\,on}$ and $\tau_{2,\,on}$ are time constants associated with the vertical doping stage. A_1 and A_2 are two constants with the value of A_1 typically ≈ 0.7 (**Fig. 5a**). For one-stage transistor turn-off, we described I_D as:

$$\left|I_{\mathrm{D,\,Norm}}(t)\right| = e^{-\frac{t}{\tau_{\mathrm{off}}}} \quad (4)$$

where τ_{off} is the time constant expressing vertical dedoping (**Fig. 5a**).

We next study how operating variables including potential and device geometry affect OECT switching behavior (**Fig. 5b–e** and **Supplementary Figs. 8–14**). During the *doping front propagation* stage, we find smaller t_p with shorter channel length as expected because the doping front is propagating at a relative constant speed. Surprisingly, we found t_p is relatively independent of the drain potential. This result suggests that ion transport from electrolyte into the polymer channel, instead of electronic transport from the source electrode, is limiting the front propagation speed. Indeed, we find faster front propagation (smaller t_p values) with higher gate potentials, presumably because the increased gate potential speeds up oxidation and ion injection. Furthermore, we observe smaller t_p with increased ion concentration, thinner channel active layer and for more chaotropic anions, all associated with shorter ion transport time from electrolyte into polymer channel.

In the *vertical doping* and *vertical dedoping* stages, we find a similar trend of $\tau_{1,\,on}$ and τ_{off} compared to t_p, namely, smaller $\tau_{1,\,on}$ and τ_{off} if the ion transport time from electrolyte into polymer layer is reduced (higher gate potential, increased ion concentration, thinner polymer layer and bulky anion[43,44,51]). We hypothesize that the smaller $\tau_{1,\,on}$ and τ_{off} with shorter channel length is akin to charging and discharging a

capacitor, where smaller capacitance (shorter channel length) results in faster charging and discharging. In contrast, the slower $\tau_{2,\,on}$, with the magnitude of ≈ 2-3 s, is less dependent on all operation variables. We propose that $\tau_{2,\,on}$ is associated with polymer structural relaxation or ionic/electronic charge reorganization, as recently suggested by Wu et al.[52] In addition, we noticed that when $|V_G - V_T| > |V_D|$, or when the device is operated in the linear region (shadowed area in **Fig. 5d** and **Supplementary Fig. 15**), the difference between turn-on and turn-off response time becomes smaller. This result is reasonable as the transistor behaves like a diode-like spectroelectrochemistry device when drain potential is decreased.

Finally, we demonstrate a SPICE circuit model (**Supplementary Note 5**) that incorporates a time-dependent channel resistor to reflect the asymmetric kinetics.[35,53] In summary, from a geometric perspective, shorter channel lengths, thinner polymer layers and higher gate potentials (*not* drain potentials) facilitate more rapid device switching. From the materials perspective, to improve device operation speed, one could increase ion concentration, select more chaotropic counterions, or design polymer with higher ionic conducting ability or more rigid backbones[54,55] to enable faster ion injection and minimize polymer structural relaxation. Detailed discussions on other key factors for designing faster OECTs, the comparison of existing OECT transient models, and the limitations of our model are in **Supplementary Note 6**, **Supplementary Table 4**, **Supplementary Table 5**, **Supplementary Note 7**, and **Supplementary Note 8**.

Outlook

We studied the asymmetric transient behavior of accumulation mode OECTs. This behavior, while ubiquitous in the literature, is rarely discussed, and is inconsistent with many common OECT models. Through operando optical microscopy coupled with OECT characterization, we find that OECT turn-on occurs in two temporally and spatially distinct stages: doping front propagation and vertical doping. In contrast, turn-off occurs in a single step, with the fastest dedoping occurring near the source but the kinetics varying only weakly across the channel. We identify several factors contributing to faster device turn-off including channel geometry, differences in doping and dedoping kinetics, and the physical phenomena of carrier density-dependent mobility. We then demonstrate an empirical model capturing the switching behavior of accumulation mode OECTs and provide physical interpretations to the response time constants. We further show that ion transport appears to be the limiting factor to device kinetics, and we offer guidance for engineering faster accumulation mode OECTs from both a materials and device perspective. We anticipate these results will aid in the selection of counterion chemistries and transistor geometries for specific applications and help improve future physics-based drift-diffusion models.

Acknowledgements

This paper is based on research supported primarily by the National Science Foundation, first under DMR-2003456, and then under DMR-2309577. K.Y., Z.S., and C.-Z.L. acknowledge support from the National Natural Science Foundation of China (22125901) for supporting the synthesis of the PB2T-TEG polymer. J.W.O. and C.K.L.'s contributions to P3MEEMT polymer synthesis are based in part on work supported by the National Science Foundation DMREF-1922259. Part of this work (transistor fabrication) was conducted at the Washington Nanofabrication Facility/Molecular Analysis Facility, a National Nanotechnology Coordinated Infra- structure (NNCI) site at the University of Washington with partial support from the National Science Foundation via awards NNCI-1542101 and NNCI-2025489.

Author contributions statement

J.G. and S.E.C. contributed equally to the work. J.G., S.E.C. and D.S.G. conceived the project, designed the experiments, and discussed the results together. J.G. and S.E.C. performed the experiments and analyzed the data. S.E.C. wrote the first draft and J.G. made the figures. R.G. performed the SPICE circuit modeling. C.G.B designed the preliminary microscope experiment. K.Y., Z.S., and C.-Z.L. provided the PB2T-TEG polymer. J.W.O. and C.K.L. provided the P3MEEMT polymer. J.G., S.E.C., R.G. and D.S.G. revised the manuscript with input from all the authors.

Competing interests statement

The authors declare no competing interests.

Figure legends/captions

Fig. 1 | OECT response times. a, Transient response of a typical accumulation mode OECT (solid) and the fit with Bernards model (dashed). The initial stage of transistor turn-on and turn-off are magnified for clarification. **b**, Accumulation mode OECT response times in literatures. Each point represents one polymer-electrolyte pair. Detailed response times and references are listed in **Supplementary Table 1**. The device response times measured in this work with carefully chosen gate voltage considering threshold voltage are represented as star symbols, which are PB2T-TEG (0.1 M KCl), P3MEEMT (0.1 M KCl), P3MEEMT (0.1 M KTFSI) and P3HT (0.1 M KTFSI). Solid and unfilled stars represent devices operated in 0.1 M KCl electrolyte and 0.1M KTFSI electrolyte, respectively.

Fig. 2 | Comparison between OECT and UV-Vis spectroelectrochemistry. a,**b**, Schematic diagram of spectroelectrochemistry (SpecEChem) (a) and OECT (b) experimental setups. **c**,**d**, Typical UV-Vis spectra (c) and OECT output curves (d) of two steady-states (neutral/doped). **e**,**f**, An example transient response of spectroelectrochemistry (**e**) at polaron peak absorption wavelength (680 nm) and OECT (**f**) at saturation region (V_D = −0.6 V). **g**,**h**, The $\tau_{doping}/\tau_{dedoping}$ measured in spectroelectrochemistry (**g**) and the τ_{on}/τ_{off} measured in OECT (**h**) for: PB2T-TEG and P3MEEMT with 0.1 M KCl (solid); P3MEEMT and P3HT with 0.1 M KTFSI (unfilled) The doping-voltage for spectroelectrochemistry, V_{doping} = OCP + 0.2 V, and the dedoping-voltage, $V_{dedoping}$ = OCP − 0.2 V. The on-voltage for OECT, V_{on} = V_T − 0.2 V, and the off-voltage, V_{off} = V_T + 0.2 V. Time resolution of spectroelectrochemistry is ≈ 10 ms and OECT is ≈ 10 μs. Error bars represent standard error of the mean from multiple cycles. We found the time constants difference between the first three consecutive cycles is small to negligible for the selected polymers (see **Supplementary Fig. 4**). For the OECT transient measurements, V_D was kept on from 0 s to 30 s while V_G was applied at 10 s (V_{on}) and removed at 20 s (V_{off}). OCP and V_T values are listed in **Supplementary Table 2.**

Fig. 3 | Operando optical microscope coupled with OECT switching. a, Operando optical microscope setup schematics. **b**, Potential and current response during turn-on. **c**, Microscope movie screenshots during turn-on with timestamp labels. Darker pixel represents higher polaron concentration. **d**, Normalized polaron absorption along channel over time during *doping front propagation* stage (stage 1 in turn-on). **e**, Comparison of I_D and moving front position over time during *doping front propagation* stage. **f**, Normalized polaron absorption along channel over time during *vertical doping* stage (stage 2 in turn-on). **g**, Comparison of I_D and normalized polaron absorption over time at selected positions during *vertical doping* stage. The solid lines indicate the fits. The insert image shows the selected positions over the channel. **h**, Potential and current response during turn-off. **i**, Microscope movie screenshots during turn-off with timestamp labels. **j**, Normalized polaron absorption along channel over time during turn-off, or *vertical dedoping*. **k**, Comparison of normalized I_D and normalized polaron absorption at three selected positions over time. The insert image shows the selected positions over the channel (labeled as source, center and drain). A 650 nm long pass filter was used, and the red channel intensity is used to calculate the polaron absorbance. The polymer used here is PB2T-TEG, and the electrolyte is 0.1 M KCl. The transistor channel length is 600 μm, and the film thickness is ≈ 120 nm. The drain potential is fixed at -0.6 V. We note that V_D is applied and kept constant before applying V_G, simulating the case of transistor operation where the V_G is switching the source-drain channel on and off.

Fig. 4 | OECT mobility and carrier density. **a**, Transient response of I_D, carrier density and average carrier mobility during the PB2T-TEG transistor turn-off. Solid line indicates the fit with biexponential equation. **b**, Calculated carrier mobility as a function of carrier density using eqn (1). Solid line indicates the fit with the eqn (2). The good fit of the classic density-dependent mobility formula to the experimental data based

on the measured current and carrier density suggests the importance of carrier density-dependent mobility in explaining the rapid turn-off of OECTs.

Fig. 5 | Dependency of OECT response times on the operation variables. a, Transient response of a typical accumulation mode PB2T-TEG OECT and the fitting equations. **b**, Relation between time constants and channel length. **c**, Relation between time constants and ion concentration. **d**, Relation between time constants and V_D. **e**, Relation between time constants and $|V_G - V_T|$. Transistor channel width is 2.5 or 5 mm, and the thickness is ≈50 nm for all cases. Electrolyte is 0.1 M KCl and transistor channel length is 100 μm unless otherwise specified. V_D is −0.6 V and $|V_G - V_T|$ is 0.2 V unless otherwise specified. Error bars are standard error of the mean from at least 3 different devices. Dashed lines are guide to the eye.

References

1. Guo, K. *et al.* Rapid single-molecule detection of COVID-19 and MERS antigens via nanobody-functionalized organic electrochemical transistors. *Nat. Biomed. Eng. 2021 57* **5**, 666–677 (2021).

2. Bischak, C. G., Flagg, L. Q. & Ginger, D. S. Ion Exchange Gels Allow Organic Electrochemical Transistor Operation with Hydrophobic Polymers in Aqueous Solution. *Adv. Mater.* **32**, 2002610 (2020).

3. Strakosas, X., Bongo, M. & Owens, R. M. The organic electrochemical transistor for biological applications. *J. Appl. Polym. Sci.* **132**, 41735 (2015).

4. Pappa, A. M. *et al.* Organic Transistor Arrays Integrated with Finger-Powered Microfluidics for Multianalyte Saliva Testing. *Adv. Healthc. Mater.* **5**, 2295–2302 (2016).

5. Huang, W. *et al.* Vertical organic electrochemical transistors for complementary circuits. *Nature* **613**, 496–502 (2023).

6. Andersson Ersman, P. *et al.* All-printed large-scale integrated circuits based on organic electrochemical transistors. *Nat. Commun.* **10**, 1–9 (2019).

7. Fuller, E. J. *et al.* Parallel programming of an ionic floating-gate memory array for scalable neuromorphic computing. *Science* **364**, 570–574 (2019).

8. Harikesh, P. C. *et al.* Ion-tunable antiambipolarity in mixed ion–electron conducting polymers enables biorealistic organic electrochemical neurons. *Nat. Mater.* **22**, 242–248 (2023).

9. Chen, S. E., Giridharagopal, R. & Ginger, D. S. Artificial neuron transmits chemical signals. *Nat. Mater.* **22**, 416–418 (2023).

10. Sarkar, T. *et al.* An organic artificial spiking neuron for in situ neuromorphic sensing and biointerfacing. *Nat. Electron.* **5**, 774–783 (2022).

11. Yamamoto, S. & Malliaras, G. G. Controlling the Neuromorphic Behavior of Organic Electrochemical Transistors by Blending Mixed and Ion Conductors. *ACS Appl. Electron. Mater.* **2**, 2224−2228 (2020).

12. Gkoupidenis, P., Schaefer, N., Garlan, B. & Malliaras, G. G. Neuromorphic Functions in PEDOT:PSS Organic Electrochemical Transistors. *Adv. Mater.* **27**, 7176–7180 (2015).

13. Khodagholy, D. *et al.* High transconductance organic electrochemical transistors. *Nat. Commun.* **4**, 2133 (2013).

14. Lin, P., Yan, F. & Chan, H. L. W. Ion-Sensitive Properties of Organic Electrochemical Transistors. *Appl. Mater. Interfaces* **2**, 1637–1641 (2010).

15. Ghittorelli, M. *et al.* High-sensitivity ion detection at low voltages with current-driven organic electrochemical transistors. *Nat. Commun.* **9**, 1441 (2018).

16. Gualandi, I. *et al.* Selective detection of dopamine with an all PEDOT:PSS Organic Electrochemical Transistor. *Sci. Rep.* **6**, 35419 (2016).

17. Xie, K. *et al.* Organic electrochemical transistor arrays for real-time mapping of evoked neurotransmitter release in vivo. *Elife* **9**, 1–19 (2020).

18. Khodagholy, D. *et al.* In vivo recordings of brain activity using organic transistors. *Nat. Commun.* **4**, (2013).

19. Tang, X., Shen, H., Zhao, S., Li, N. & Liu, J. Flexible brain-computer interfaces. *Nat. Electron.* **6**, 109–118 (2023).

20. Berggren, M., Głowacki, E. D., Simon, D. T., Stavrinidou, E. & Tybrandt, K. In Vivo Organic Bioelectronics for Neuromodulation. *Chem. Rev.* **122**, 4826–4846 (2022).

21. Go, G.-T., Lee, Y., Seo, D.-G. & Lee, T.-W. Organic Neuroelectronics: From Neural Interfaces to Neuroprosthetics. *Adv. Mater.* **34**, 2201864 (2022).

22. Van DeBurgt, Y., Melianas, A., Keene, S. T., Malliaras, G. & Salleo, A. Organic electronics for neuromorphic computing. *Nat. Electron.* **1**, 386–397 (2018).

23. Gumyusenge, A., Melianas, A., Keene, S. T. & Salleo, A. Materials Strategies for Organic Neuromorphic Devices. *Annu. Rev. Mater. Res.* **51**, 1–25 (2021).

24. Rivnay, J. *et al.* Organic electrochemical transistors. *Nat. Rev. Mater.* **3**, 17086 (2018).

25. Zeglio, E. & Inganäs, O. Active Materials for Organic Electrochemical Transistors. *Adv. Mater.* **30**, 1800941 (2018).

26. Kukhta, N. A., Marks, A. & Luscombe, C. K. Molecular Design Strategies toward Improvement of Charge Injection and Ionic Conduction in Organic Mixed Ionic-Electronic Conductors for Organic Electrochemical Transistors. *Chem. Rev.* **122**, 4325–4355 (2022).

27. He, Y., Kukhta, N. A., Marks, A. & Luscombe, C. K. The effect of side chain engineering on conjugated polymers in organic electrochemical transistors for bioelectronic applications. *J. Mater. Chem. C* **10**, 2314–2332 (2022).

28. Paulsen, B. D., Tybrandt, K., Stavrinidou, E. & Rivnay, J. Organic mixed ionic–electronic conductors. *Nat. Mater.* **19**, 13–26 (2020).

29. Flagg, L. Q. *et al.* P-Type Electrochemical Doping Can Occur by Cation Expulsion in a High-Performing Polymer for Organic Electrochemical Transistors. *ACS Mater. Lett.* **2**, 254–260 (2020).

30. Bernards, D. A. & Malliaras, G. G. Steady-state and transient behavior of organic electrochemical transistors. *Adv. Funct. Mater.* **17**, 3538–3544 (2007).

31. Ohayon, D., Druet, V. & Inal, S. A guide for the characterization of organic electrochemical transistors and channel materials. *Chem. Soc. Rev.* 1001–1023 (2023).

32. Inal, S., Malliaras, G. G. & Rivnay, J. Benchmarking organic mixed conductors for transistors. *Nat. Commun.* **8**, 1767 (2017).

33. Li, P. & Lei, T. Molecular design strategies for high-performance organic electrochemical transistors. *J. Polym. Sci.* **60**, 377–392 (2022).

34. Gentile, F. *et al.* A theoretical model for the time varying current in organic electrochemical transistors in a dynamic regime. *Org. Electron.* **35**, 59–64 (2016).

35. Faria, G. C., Duong, D. T. & Salleo, A. On the transient response of organic electrochemical transistors. *Org. Electron.* **45**, 215–221 (2017).

36. Paudel, P. R. *et al.* The Transient Response of Organic Electrochemical Transistors. *Adv. Theory Simul.* 2100563 (2022).

37. Keene, S. T. *et al.* Hole-limited electrochemical doping in conjugated polymers. *Nat. Mater.* **22**, 1121–1127 (2023).

38. Ersman, P. A. *et al.* Screen printed digital circuits based on vertical organic electrochemical transistors. *Flex. Print. Electron.* **2**, 045008 (2017).

39. Butler, J. A. V. Studies in heterogeneous equilibria. Part II. - The kinetic interpretation of the nernst theory of electromotive force. *Trans. Faraday Soc.* **19**, 729–733 (1924).

40. Butler, J. A. V. Studies in heterogeneous equilibria. Part III. A kinetic theory of reversible oxidation potentials at inert electrodes. *Trans. Faraday Soc.* **19**, 734–739 (1924).

41. Erdey-Grúz, T. & Volmer, M. Zur Theorie der Wasserstoff Überspannung. *Zeitschrift für Phys. Chemie* **150A**, 203–213 (1930).

42. Bischak, C. G. *et al.* A Reversible Structural Phase Transition by Electrochemically- Driven Ion Injection into a Conjugated Polymer. *J. Am. Chem. Soc.* **142**, 7434−7442 (2020).

43. Flagg, L. Q. *et al.* Polymer Crystallinity Controls Water Uptake in Glycol Side-Chain Polymer Organic Electrochemical Transistors. *J. Am. Chem. Soc.* **141**, 4345–4354 (2019).

44. Chen, S. E. *et al.* Impact of varying side chain structure on organic electrochemical transistor performance: a series of oligoethylene glycol-substituted polythiophenes †. *J. Mater. Chem. A* **10**, 10738–10749 (2022).

45. Neusser, D. *et al.* High Conductivities of Disordered P3HT Films by an Electrochemical Doping Strategy. *Chem. Mater* **32**, 6003–6013 (2020).

46. Hornberger, L. S., Neusser, D., Malacrida, C., Kaake, L. G. & Ludwigs, S. How charge trapping affects the conductivity of electrochemically doped poly(3-hexylthiophene) films. *Appl. Phys. Lett.* **119**, 163301 (2021).

47. Jackson, S. R., Kingsford, R. L., Collins, G. W. & Bischak, C. G. Crystallinity Determines Ion Injection Kinetics and Local Ion Density in Organic Mixed Conductors. *Chem. Mater.* **35**, 5400 (2023).

48. Friedlein, J. T., Shaheen, S. E., Malliaras, G. G. & McLeod, R. R. Optical Measurements Revealing Nonuniform Hole Mobility in Organic Electrochemical Transistors. *Adv. Electron. Mater.* **1**, 1500189 (2015).

49. Tanase, C., Meijer, E. J., Blom, P. W. M. & DeLeeuw, D. M. Unification of the Hole Transport in Polymeric Field-Effect Transistors and Light-Emitting Diodes. *Phys. Rev. Lett.* **9**, 216601 (2003).

50. Bässler, H., Kroh, D., Schauer, F., Nádaždy, V. & Köhler, A. Mapping the Density of States Distribution of Organic Semiconductors by Employing Energy Resolved–Electrochemical Impedance Spectroscopy. *Adv. Funct. Mater.* **31**, (2021).

51. Flagg, L. Q., Giridharagopal, R., Guo, J. & Ginger, D. S. Anion-Dependent Doping and Charge Transport in Organic Electrochemical Transistors. *Chem. Mater.* **30**, 5380–5389 (2018).

52. Wu, R., Paulsen, B. D., Ma, Q. & Rivnay, J. Mass and Charge Transport Kinetics in an Organic Mixed Ionic−Electronic Conductor. *Chem. Mater.* **34**, 9699–9710 (2022).

53. Colucci, R., Barbosa, H. F. D. P., Günther, F., Cavassin, P. & Faria, G. C. Recent advances in modeling organic electrochemical transistors. *Flex. Print. Electron.* **5**, 013001 (2020).

54. Guo, J. *et al.* Hydration of a Side-Chain-Free n-Type Semiconducting Ladder Polymer Driven by Electrochemical Doping. *J. Am. Chem. Soc.* **145**, 1866–1876 (2023).

55. West, S. M. *et al.* Phenazine-Substituted Poly(benzimidazobenzophenanthrolinedione): Electronic Structure, Thin Film Morphology, Electron Transport, and Mechanical Properties of an n-Type Semiconducting Ladder Polymer. *Macromolecules* **56**, 2081–2091 (2023).

Methods

Polymer film preparation and characterization

The synthesis of PB2T-TEG[1,2] (see detailed molecular weight information in the previous paper[2]) and P3MEEMT[3] (M_n = 24 kg/mol, $Đ$ = 1.67) polymers were described in our previous works. P3HT was obtained from Ossila (M109, M_w =36.6 kg/mol). PB2T-TEG polymer was dissolved in chloroform with the concentration of 2 to 4.5 mg/mL. P3MEEMT and P3HT polymers were dissolved in chlorobenzene with the concentration of 20 mg/mL. All polymer solutions were stirred overnight at 50 °C prior to spin coating. The substrates were cleaned sequentially by sonication in acetone and isopropanol for 15 min each. The surface of the substrate was then treated with oxygen plasma for 3 min before spin coating. The spin rate used is 600–2500 rpm to control film thickness between 20 nm to 120 nm. PB2T-TEG polymer films were annealed at 150 °C for 10 minutes under N_2 after spin-coating.

OECT device fabrication and characterization

OECT devices comprised lithographically patterned gold on glass substrates (see lithography process below) with transistor widths of 2.5 mm, 5 mm or 6 mm and lengths ranging from 10 μm to 600 μm. Polymers were spun casted onto OECT substrates and were carefully removed except at the electrode junction region via cotton tips (slightly dampened with acetone solution) under microscope or magnifying lens to ensure minimum impact on the transient response. A secure seal hybridization chamber (GRACE BIO LABS) is attached onto the substrate to confine the electrolyte. A Ag/AgCl pellet is used as the gate. The distance between gate and channel is fixed at approximately 4 mm in this study. The transfer curves were measured using two Keithley 2400 source-measure units controlled by custom Python code. The transient measurements were conducted with NI PXIe-5451, NI PXIe-6366 and NI PXIe-8381 controlled by custom LabVIEW code with time resolution ≈ 10 μs. Drain potential (V_D) is typically −0.6 V for OECT experiments unless otherwise specified. We applied gate potential (V_G) in a fashion to compare transistors at fixed values of $|V_G - V_T|$, which is typically 0.2 V unless otherwise specified. For OECT transient measurements, we

kept the V_D fixed (on) while changing V_G for OECT device switching, which reflects a typical transistor application situation where the gate is being used to switch the source drain current on and off.

The detailed lithography process: NR9-3000PY negative resist (Futurrex, Inc.) was deposited on cleaned glass wafers with diameter equals to 100 mm (University Wafer, Inc.) using Rite Track Automated Coater (SVG-90S), followed by UV light exposure (ABM-SemiAuto-Aligner) and resist development (SVG-90S). Metal deposition (10 nm chromium and 100 nm gold) was accomplished through evaporation (CHA Solution e-beam evaporator). The resist lift-off was achieved by soaking wafers in acetone solution overnight. The wafers were then diced using a Disco Wafer Dicer (Disco, America).

Operando microscope coupled with OECT characterization

An iPhone 11 Pro (1080 P, 240 fps) was attached to Leica CME microscope with a 15× eyepiece, a 10× objective (NA = 0.25) and a 650 nm long pass filter (FEL0650, THORLABS) for video recording. Videos were analyzed using custom Python code with OpenCV library. A dark and a reference image were taken for dark and flat field frame corrections, and absorbance calculation. To optimize the video contrast, a thicker PB2T-TEG film was prepared by drop casting from 1 mg/mL chlorobenzene solution to slow down the evaporation rate.

Spectroelectrochemistry characterization

The ultraviolet-visible (UV-Vis) absorption spectra were measured using an AVANTES spectrometer (AvaSpec-2048L) coupled with an AVANTES light source (Avalight-HAL-S). Doping and dedoping UV-Vis spectra were collected using continuous mode (with AvaSoft software) with time resolution ≈10 ms/spectrum. The potential bias is controlled using a Metrohm Autolab PGSTAT204 (with NOVA Software version 2.1). Polymers were cast onto fluoride-doped tin oxide-coated glass (FTO, Sigma-Aldrich, 7 Ω/sq) and used as a working electrode. A Ag/AgCl electrode and a Pt mesh were used as reference electrode and counter electrode, respectively. All three electrodes were submerged into a cuvette containing ≈ 2.5 mL of either 0.1 M $KCl_{(aq)}$ or 0.1 M $KTFSI_{(aq)}$.

Data availability

The data that support the findings of this study are available within the paper and its Supplementary Information. Source data are provided with this paper. Additional data may be requested from the authors.

Methods-only references

1. Bischak, C. G. *et al.* A Reversible Structural Phase Transition by Electrochemically- Driven Ion Injection into a Conjugated Polymer. *J. Am. Chem. Soc.* **142**, 7434−7442 (2020).
2. Zhang, Z. *et al.* Modulate Molecular Interaction between Hole Extraction Polymers and Lead Ions toward Hysteresis-Free and Efficient Perovskite Solar Cells. *Adv. Mater. Interfaces* **5**, 1800090 (2018).
3. Flagg, L. Q. *et al.* Polymer Crystallinity Controls Water Uptake in Glycol Side-Chain Polymer Organic Electrochemical Transistors. *J. Am. Chem. Soc.* **141**, 4345–4354 (2019).

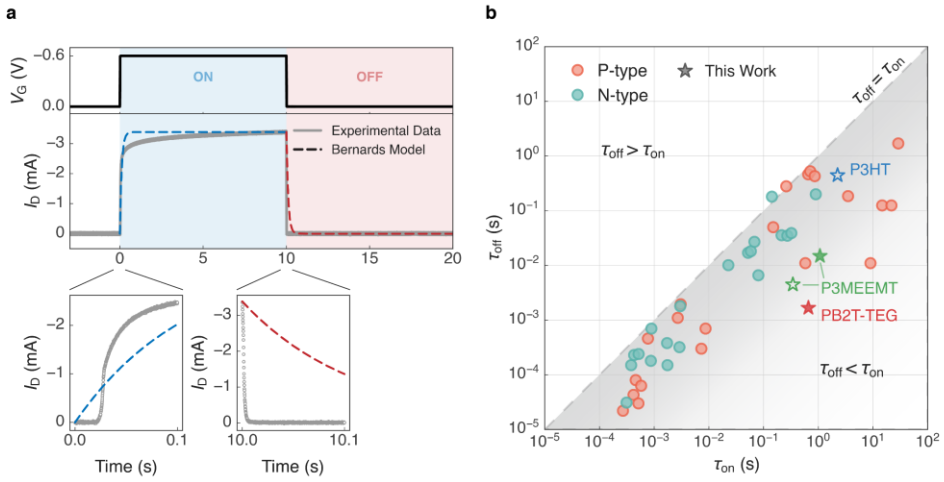
a
b
ON
OFF
Experimental Data
Bernards Model
V_G (V)
I_D (mA)
Time (s)
P-type
N-type
This Work
$\tau_{off} = \tau_{on}$
$\tau_{off} > \tau_{on}$
$\tau_{off} < \tau_{on}$
P3HT
P3MEEMT
PB2T-TEG
τ_{off} (s)
τ_{on} (s)

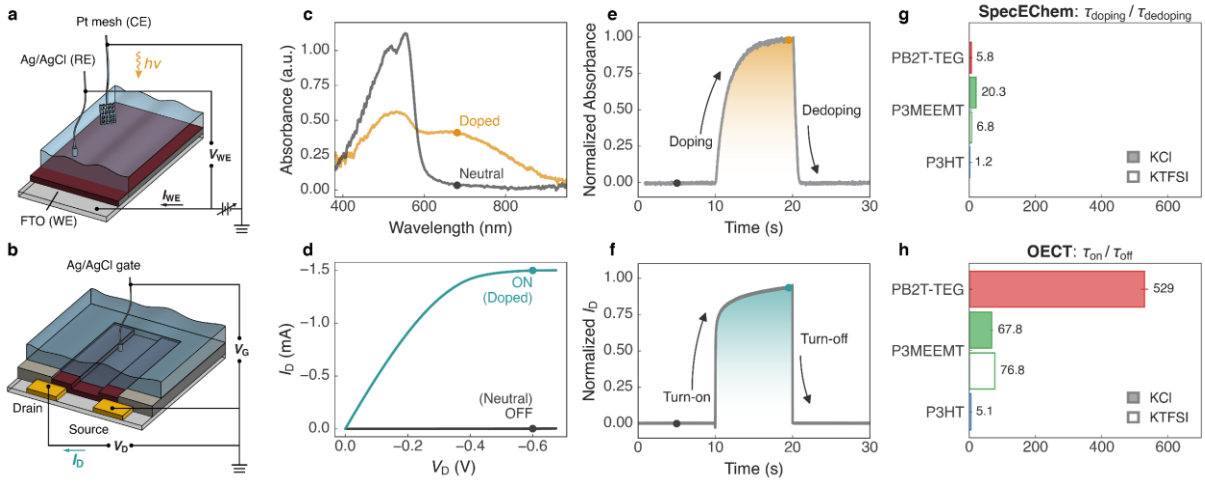
a
Pt mesh (CE)
Ag/AgCl (RE)
hν
V_{WE}
I_{WE}
FTO (WE)
b
Ag/AgCl gate
V_G
Drain
Source
V_D
I_D
c
Absorbance (a.u.)
Doped
Neutral
Wavelength (nm)
d
I_D (mA)
ON
(Doped)
(Neutral)
OFF
V_D (V)
e
Normalized Absorbance
Doping
Dedoping
Time (s)
f
Normalized I_D
Turn-on
Turn-off
Time (s)
g
SpecEChem: τ_{doping} / $\tau_{dedoping}$
PB2T-TEG
P3MEEMT
P3HT
5.8
20.3
6.8
1.2
KCl
KTFSI
h
OECT: τ_{on} / τ_{off}
PB2T-TEG
P3MEEMT
P3HT
529
67.8
76.8
5.1
KCl
KTFSI

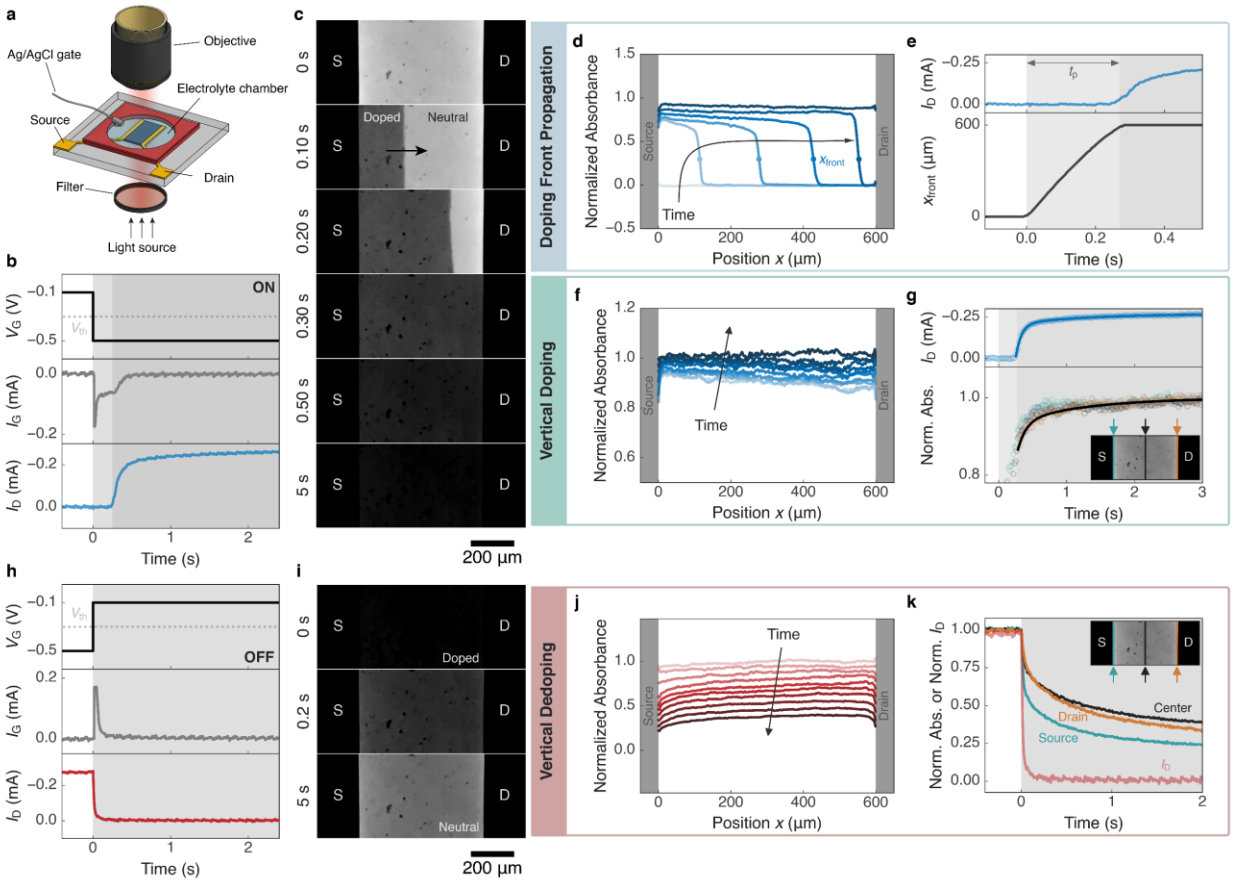
a
Ag/AgCl gate
Objective
Electrolyte chamber
Source
Drain
Filter
Light source
b
ON
OFF
V_G (V)
I_G (mA)
I_D (mA)
V_{th}
Time (s)
c
0 s
0.10 s
0.20 s
0.30 s
0.50 s
5 s
S
D
Doped
Neutral
200 µm
Doping Front Propagation
Vertical Doping
Vertical Dedoping
d
Normalized Absorbance
Source
Drain
x_{front}
Time
Position x (µm)
e
t_p
x_{front} (µm)
Time (s)
f
g
Norm. Abs.
h
i
j
k
Norm. Abs. or Norm. I_D
Center

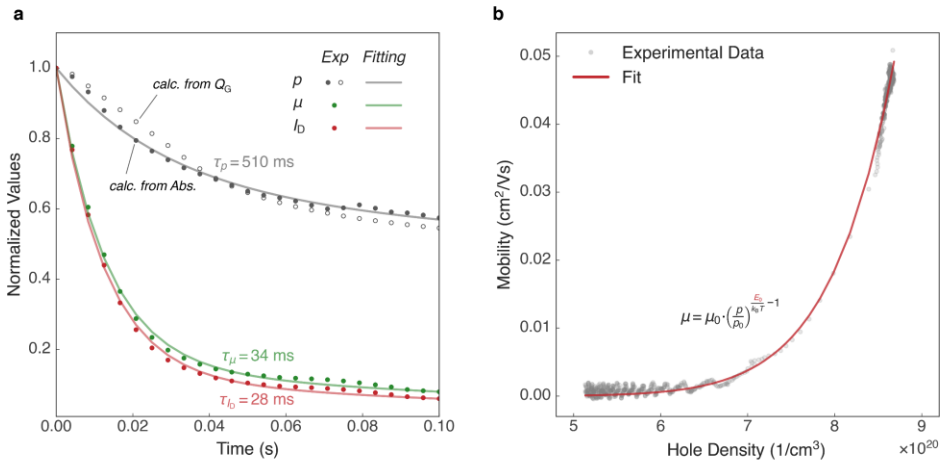
a
Exp
Fitting
p
μ
I_D
calc. from Q_G
calc. from Abs.
τ_p = 510 ms
τ_μ = 34 ms
τ_I_D = 28 ms
Normalized Values
Time (s)
b
Experimental Data
Fit
Mobility (cm²/Vs)
Hole Density (1/cm³)
×10²⁰

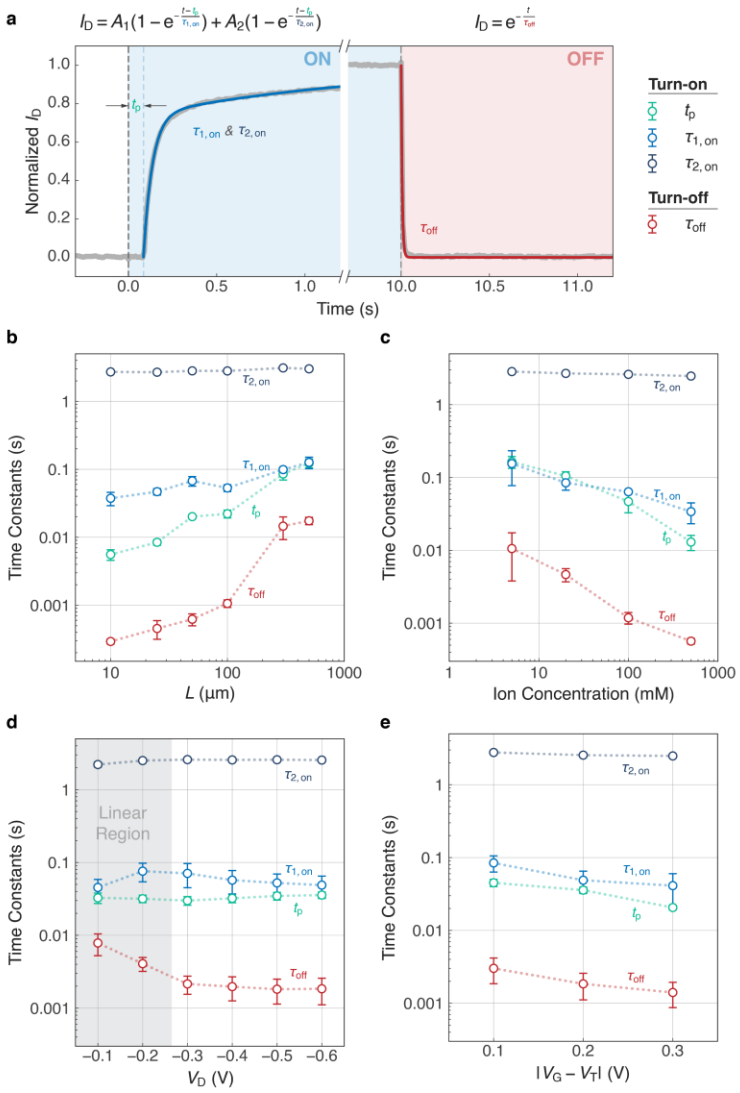
a
$I_D = A_1(1 - e^{-\frac{t-t_p}{\tau_{1,on}}}) + A_2(1 - e^{-\frac{t-t_p}{\tau_{2,on}}})$
$I_D = e^{-\frac{t}{\tau_{off}}}$
ON
OFF
Normalized I_D
t_p
$\tau_{1,on}$ & $\tau_{2,on}$
τ_{off}
Time (s)
Turn-on
t_p
$\tau_{1,on}$
$\tau_{2,on}$
Turn-off
τ_{off}
b
Time Constants (s)
L (μm)
c
Time Constants (s)
Ion Concentration (mM)
d
Linear Region
Time Constants (s)
V_D (V)
e
Time Constants (s)
$|V_G - V_T|$ (V)

Supplementary Figures

Supplementary Tables

Supplementary Notes

Supplementary Videos

Supplementary Video 1. *Doping video coupled with the OECT drain current.*

Supplementary Video 2. *Comparison of doping front propagation at various* V_D.

Supplementary Video 3. *5 cycles switching of PB2T-TEG.*

Supplementary Video 4. *P3MEEMT switching.*

Supplementary Video 5. V_D *and* V_G *applied at the same time during transistor turn-on.*

Supplementary Video 6. *Dedoping video coupled with the OECT drain current.*

References

Supplementary Figures

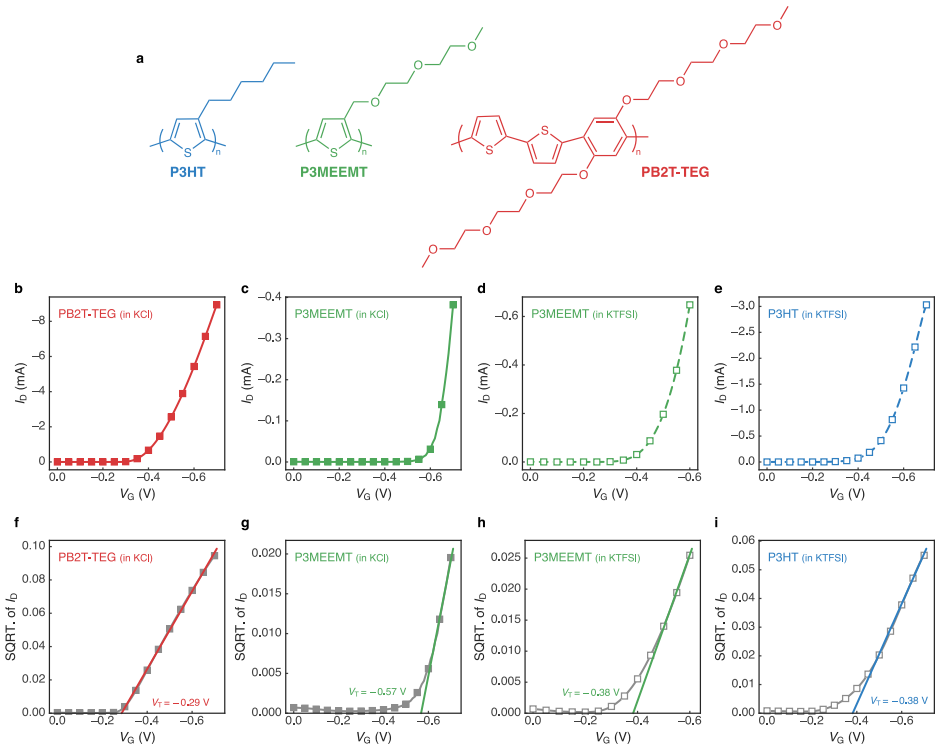

Supplementary Figure 1. Transfer curves and threshold voltage determination. (a) The polymer structure of P3HT, P3MEEMT, and PB2T-TEG (b-e) transfer curves and (e-i) threshold voltage fits of polymers in 0.1 M KCl and 0.1 M KTFSI.

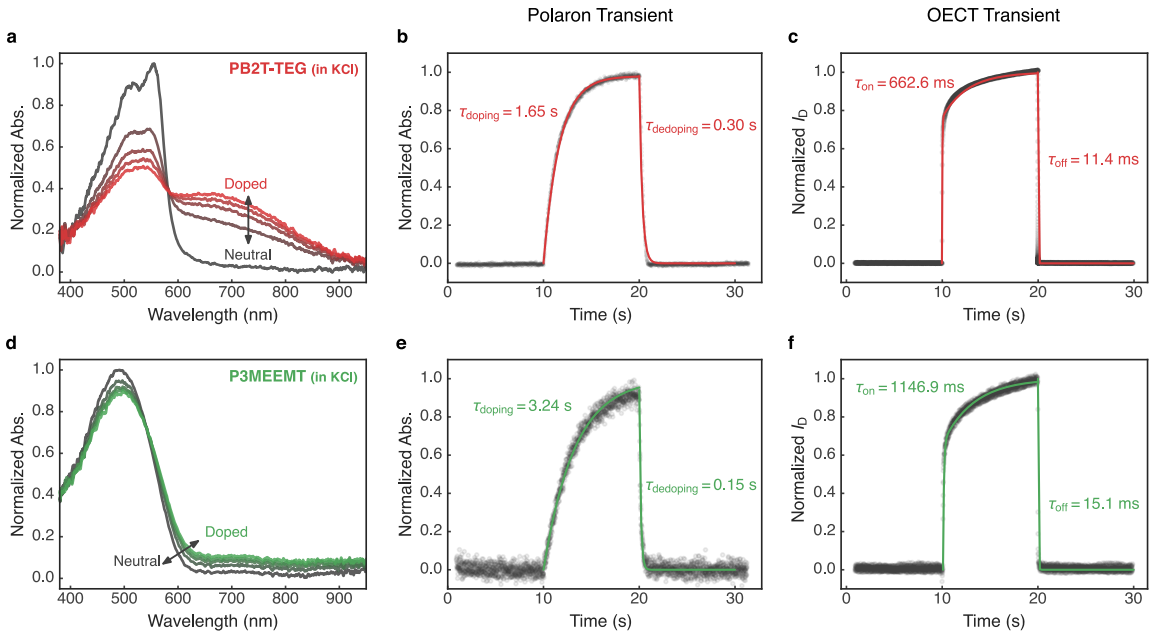

Supplementary Figure 2. The comparison between spectroelectrochemistry and OECT transient behaviors in 0.1 M KCl. The UV-Vis spectra of (a) PB2T-TEG and (d) P3MEEMT in 0.1 M KCl. The Polaron transient of (b) PB2T-TEG and (e) P3MEEMT in 0.1 M KCl. The OECT transient of (c) PB2T-TEG and (f) P3MEEMT in 0.1 M KCl. Dots represent the data and lines represent the fit in (b), (c), (e), and (f).

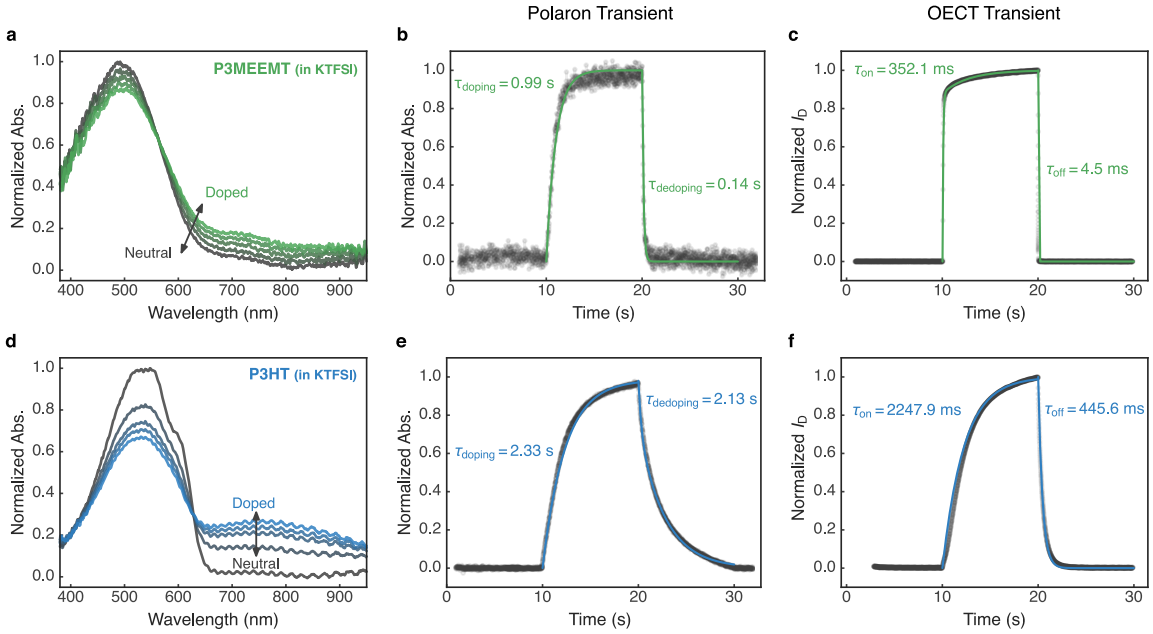

Supplementary Figure 3. The comparison between spectroelectrochemistry and OECT transient behaviors in 0.1 M KTFSI. The UV-Vis spectra of (a) PB2T-TEG and (d) P3MEEMT in 0.1 M KTFSI. The polaron transient of (b) PB2T-TEG and (e) P3MEEMT in 0.1 M KTFSI. The OECT transient of (c) PB2T-TEG and (f) P3MEEMT in 0.1 M KTFSI. Dots represent the data and lines represent the fit in (b), (c), (e), and (f).

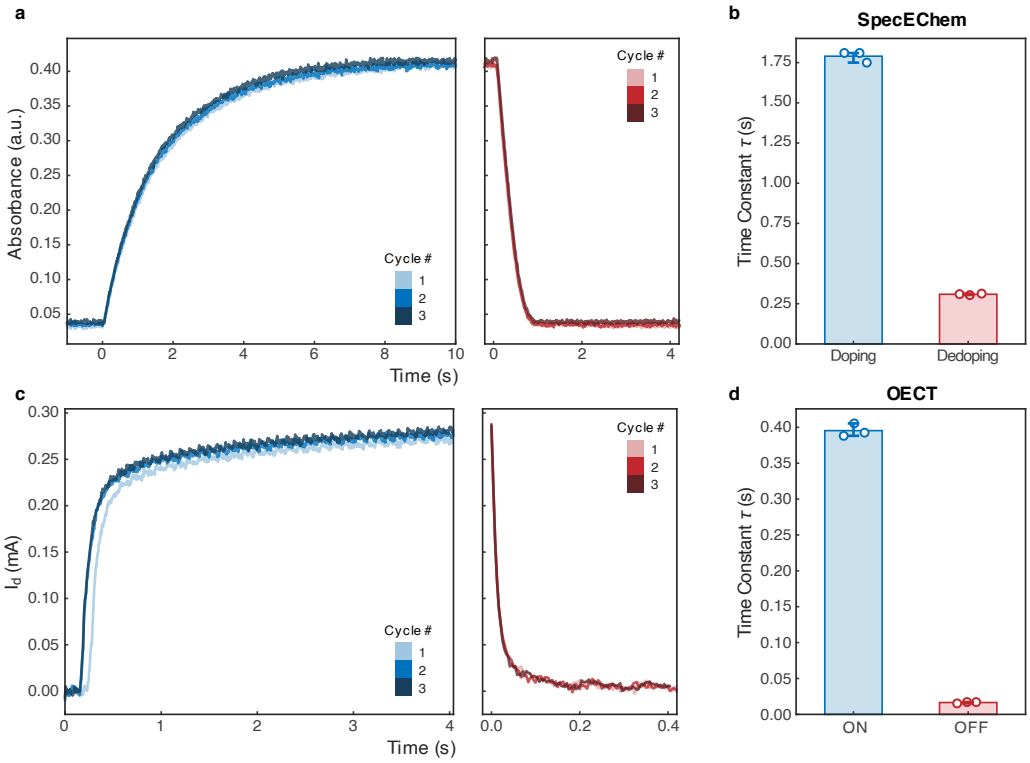

Supplementary Figure 4. Comparison of time constants between different cycles. Overlay of the transient response of three consecutive cycles in (a) OECT and (c) Spectroelectrochemistry. Comparison of the time constants of three consecutive cycles in (b) OECT and (d) Spectroelectrochemistry. The measure of centers indicate the average time constants and error bars represent the standard deviation (cycle number = 3). The polymer shown here is PB2T-TEG and the electrolyte is 0.1 M KCl.

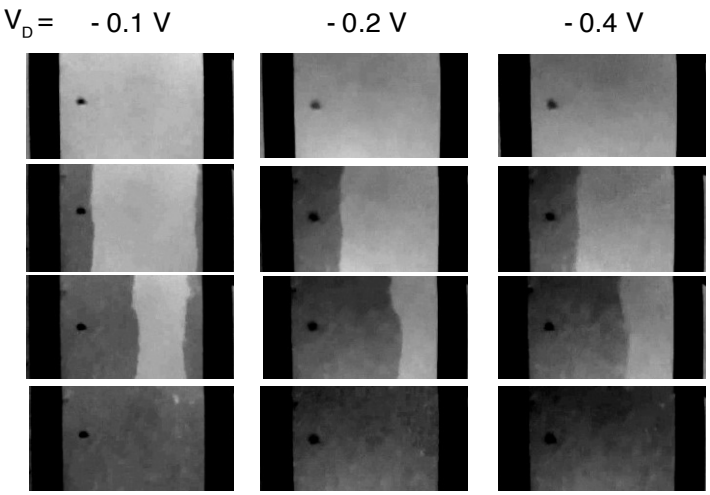

Supplementary Figure 5. Microscope screenshots of PB2T-TEG OECT channels during operation with different V_D. Turn-on process with the drain voltage V_D of – 0.1 V (left), – 0.2 V (middle) and – 0.4 V (right). The video was captured with a 650 nm long pass filter. Darker pixels represent higher polaron concentration.

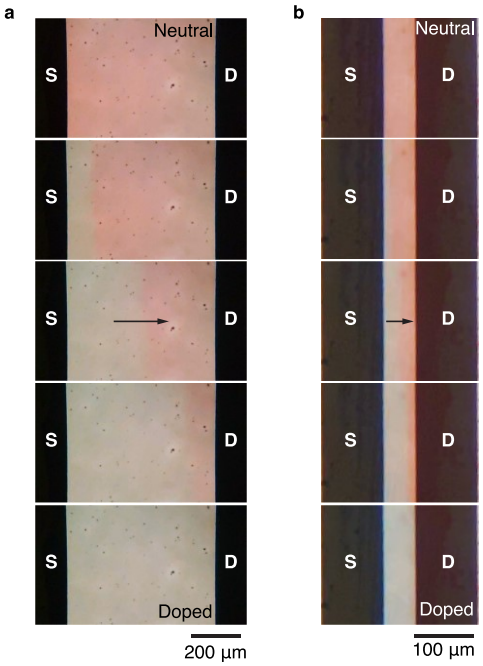

Supplementary Figure 6. Microscope screenshots of P3MEEMT OECT channels during operation. Turn-on process of P3MEEMT-based OECT with the channel length of (a) 600 µm (b) 50 µm. The electrolyte is 0.1 M KCl. Arrows indicate the doping front propagation direction. The color of the P3MEEMT polymer is red/orange in the neutral state and blue in the doped state.

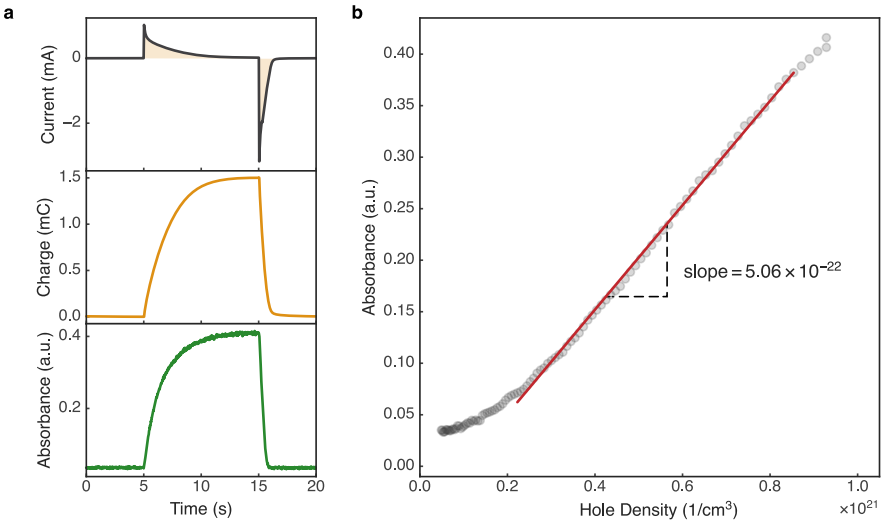

Supplementary Figure 7. The absorption-hole density calibration based on Beer's law. (a) The transient response of current, charge, and absorbance of PB2T-TEG in spectroelectrochemistry. The electrolyte is 0.1 M KCl. (b) The relation between absorbance and hole density.

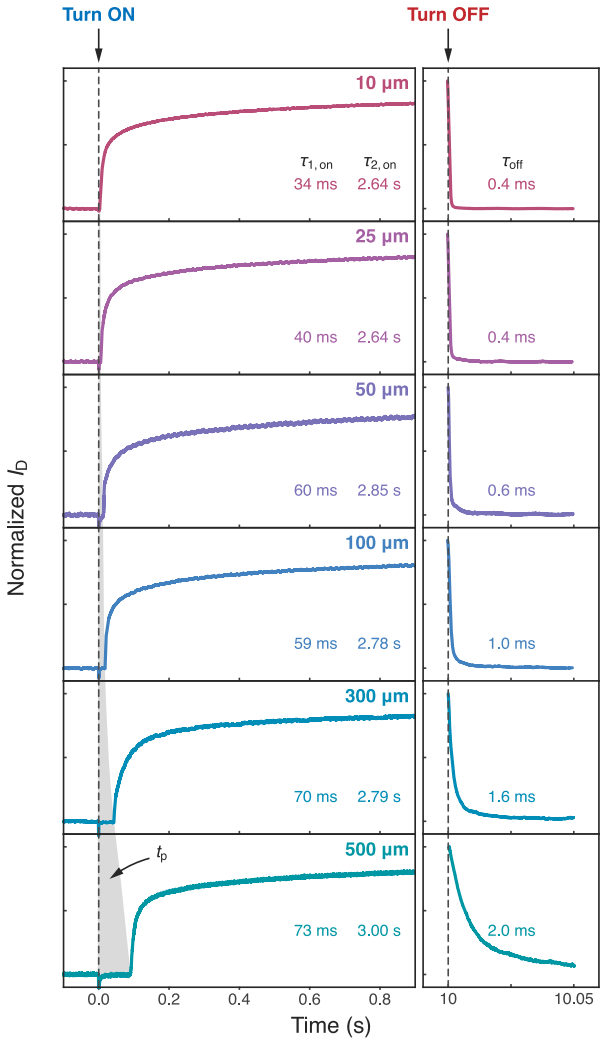

Supplementary Figure 8. The transient response with various channel lengths. The polymer is PB2T-TEG, and the electrolyte is 0.1 M KCl. The transistor channel width is 5 mm and the film thickness is ≈ 50 nm. The gate potential is fixed at $|V_G - V_T| = 0.2$ V, and the drain potential is – 0.6 V.

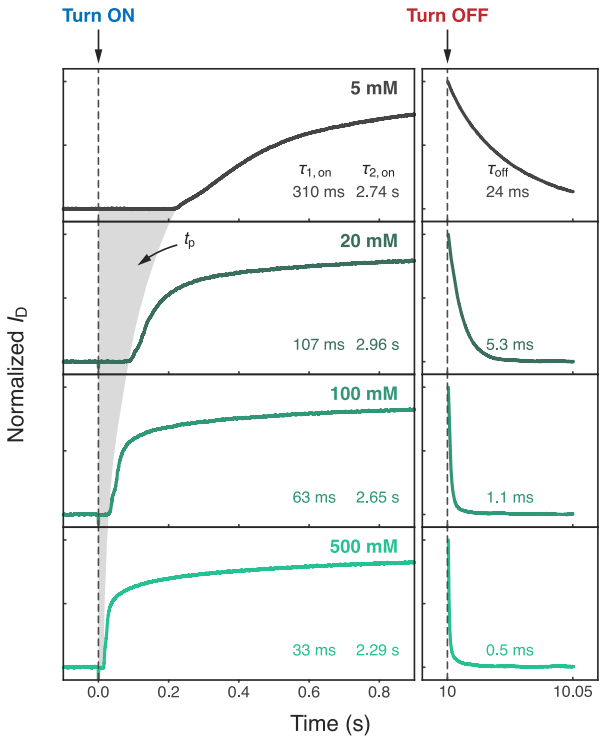

Supplementary Figure 9. The transient response with various ion concentrations. The polymer is PB2T-TEG. The transistor channel width is 2.5 mm, the channel length is 100 μm and the film thickness is ≈ 50 nm. The gate potential is fixed at $|V_G - V_T| = 0.2$ V, and the drain potential is – 0.6 V.

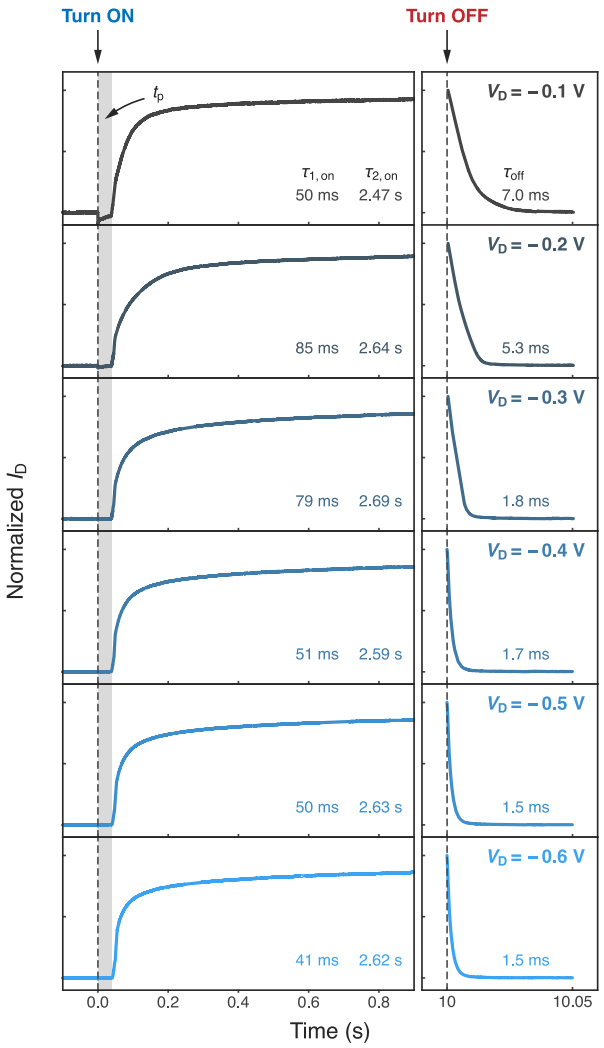

Supplementary Figure 10. The transient response with various drain potentials. The polymer is PB2T-TEG, and the electrolyte is 0.1 M KCl. The transistor channel width is 5 mm, the channel length is 100 μm, and the film thickness is ≈ 50 nm. The gate potential is fixed at $|V_G - V_T| = 0.2$ V.

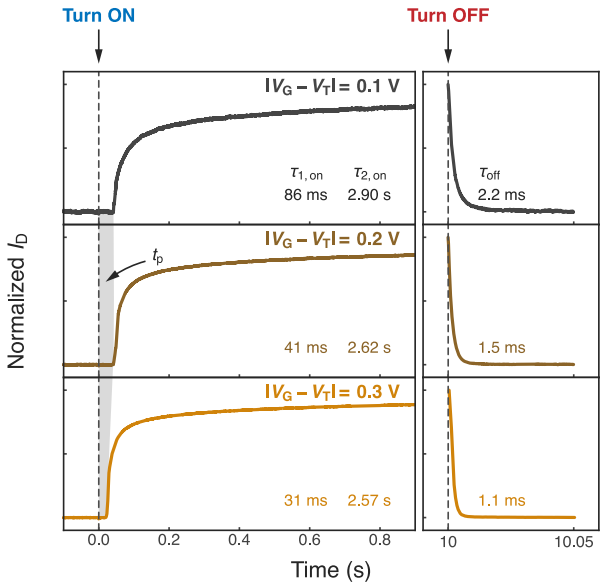

Supplementary Figure 11. The transient response with various gate potentials. The polymer is PB2T-TEG, and the electrolyte is 0.1 M KCl. The transistor channel width is 5 mm, the channel length is 100 μm, and the film thickness is ≈ 50 nm. The drain potential is – 0.6 V.

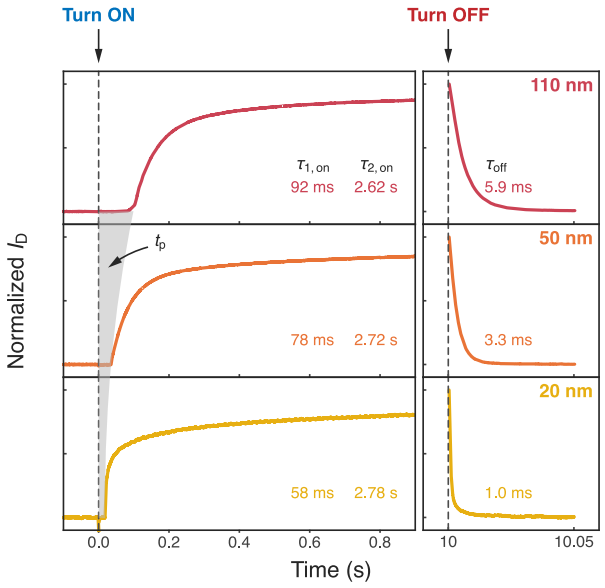

Supplementary Figure 12. The transient response with various film thickness. The polymer is PB2T-TEG, and the electrolyte is 0.1 M KCl. The transistor channel width is 5 mm, and the channel length is 100 μm. The gate potential is fixed at $|V_G - V_T| = 0.2$ V, and the drain potential is – 0.6 V.

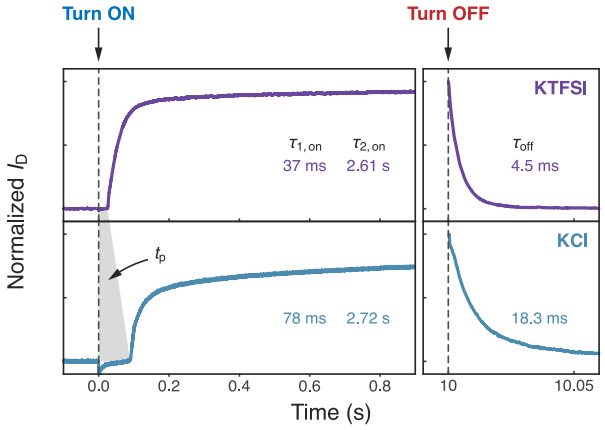

Supplementary Figure 13. The transient response with various counter anion species. The polymer is P3MEEMT. The transistor channel width is 5 mm, the channel length is 100 μm, and the film thickness is ≈ 120 nm. The gate potential is fixed at $|V_G - V_T| = 0.2$ V, and the drain potential is – 0.6 V.

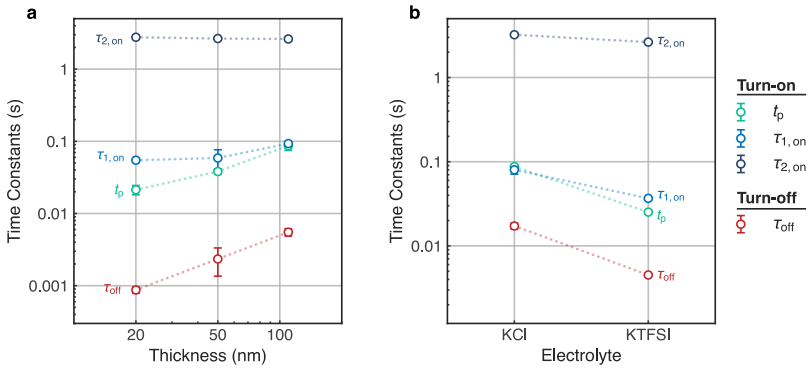

Supplementary Figure 14. The relation between response time constants and (a) thickness and (b) counter anions. Thickness results are from **Supplementary Figure 13** and counter anions results are from **Supplementary Figure 12**). The measure of centers indicate the mean time constants from multiple cycles and error bars represent the standard error of the mean (cycle number = 3).

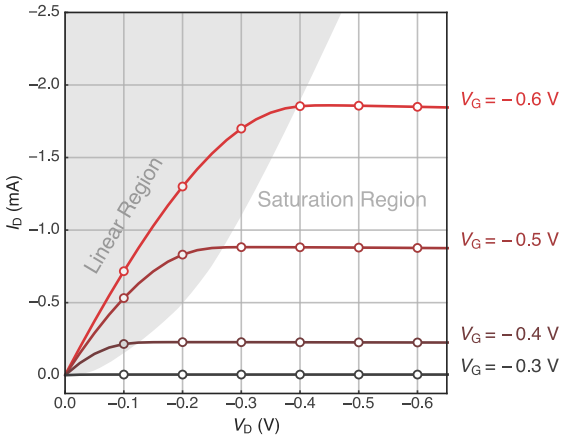

Supplementary Figure 15. The output curve of PB2T-TEG in 0.1 M KCl.

Supplementary Tables

Supplementary Table 1. Accumulation mode OECT response times in literatures

The graph of the response times is shown in the main manuscript **Figure 1B**. We considered published results with typical planar structure and aqueous electrolyte, which is the most common OECT structure to date.

Polymer	Type	Ion Concentration (mM)	Ion Type	τon (ms)	τoff (ms)	Reference	Note
gDPP-g2T	p	PBS buffer	PBS buffer	0.269	0.022	[1]	cOECT
p(g2T-TT)	p	100	NaCl	0.42	0.043	[2]	
P(gTDPPT)	p	100	NaCl	0.46	0.08	[3]	
P(bgDPP-MeOT2)	p	100	NaCl	0.516	0.03	[4]	
P(lgDPP-MeOT2)	p	100	NaCl	0.578	0.063	[4]	
p(gPyDPP-MeOT2)	p	100	NaCl	0.77	0.46	[5]	
PBBTL	p	100	NaCl	2.7	1.1	[6]	
PBBTL/BBL blend	p	100	NaCl	3.05	1.95	[6]	
TDPP-gTVT	p	100	NaCl	7.3	0.3	[7]	
TDPP-gTBTT	p	100	NaCl	8.7	0.7	[7]	
PProDOT-DPP	p	100	LiCl	150	50	[8]	
PProDOT-DPP	p	100	LiPF6	260	280	[8]	
P3APPT	p	100	KPF6	580	11	[9]	estimation
PIBET-AO	p	50	KCl + CaCl2	654	463	[10]	
PIBET-O	p	50	KCl + CaCl2	714	526	[10]	
PIBET-BO	p	50	KCl + CaCl2	862	429	[10]	
PIBT-BO	p	50	KCl + CaCl2	3500	185	[10]	
P3APPT	p	100	KCl	9000	11	[9]	estimation
DPP-DTT (8:2)	p	100	KPF6	14705	125	[11]	400 μm, estimation
DPP-DTT (1:0)	p	100	KPF6	21739	125	[11]	400 μm, estimation
PIBET-A	p	50	KCl + CaCl2	29000	1700	[10]	
Polymer	**Type**	**Ion Concentration (mM)**	**Ion Type**	**τon (ms)**	**τoff (ms)**	**Reference**	**Note**
Homo-gDPP	n	PBS buffer	PBS buffer	0.313	0.031	[1]	cOECT
BBL152	n	100	NaCl	0.38	0.15	[12]	
BBL98	n	100	NaCl	0.43	0.23	[12]	
BBL60	n	100	NaCl	0.52	0.24	[12]	
gNDI-T	n	100	KCl	0.87	0.18	[13]	normalized to area
BBL15	n	100	NaCl	0.89	0.7	[12]	
PBBTL/BBL blend	n	100	NaCl	1.72	0.38	[6]	
P(gTDPP2FT)	n	100	NaCl	1.75	0.15	[3]	
gNDI-V	n	100	KCl	2.9	0.32	[13]	normalized to area
P(gPzDPP-CT2)	n	100	NaCl	3	1.8	[14]	
P(gPzDPP-2T)	n	100	NaCl	22.7	10.1	[14]	
f-BTI2g-TVTCN	n	100	NaCl	52	17	[15]	
gAIID-2FT	n	100	NaCl	58.5	18.2	[16]	
f-BTI2g-TVT	n	100	NaCl	68	27	[15]	
BBLH	n	100	KCl	80.3	6.6	[17]	

BBLL	n	100	KCl	142	181	[17]	
gAIID-T	n	100	NaCl	213.3	35.6	[16]	
f-BTI2TEG-FT	n	100	NaCl	272	35	[18]	
f-BTI2TEG-T	n	100	NaCl	322	39	[18]	
BBL	n	100	NaCl	900	200	[19]	estimation

Supplementary Table 2. OCP and V_T values of different polymer/electrolyte pairs

Polymer	Electrolyte	OCP (V)[a]	V_T (V)[b]
PB2T-TEG	0.1 M KCl	0.11	-0.29
P3MEEMT	0.1 M KCl	0.13	-0.57
P3MEEMT	0.1 M KTFSI	-0.03	-0.38
P3HT	0.1 M KTFSI	-0.12	-0.38

a. Open circuit potential of the system.
b. OECT threshold voltage. See **Supplementary Figure 1**.

Supplementary Table 3. Response time constants of spectroelectrochemistry (SpecEChem) and OECT

Polymer	Electrolyte	SpecEChem τ_{doping} (s) [a]	OECT τ_{on} (s) [b]	SpecEChem $\tau_{dedoping}$ (s) [c]	OECT τ_{off} (s) [d]
PB2T-TEG	0.1 M KCl	1.69 ± 0.01	0.65828 ± 0.00701	0.29 ± 0.01	0.00124 ± 0.00002
P3MEEMT	0.1 M KCl	3.17 ± 0.07	1.14873 ± 0.03257	0.16 ± 0.01	0.01693 ±0.00075
P3MEEMT	0.1 M KTFSI	1.05 ± 0.03	0.34316 ± 0.00515	0.15 ± 0.01	0.00447 ± 0.00004
P3HT	0.1 M KTFSI	2.67 ± 0.35	2.25052 ± 0.01539	2.18 ± 0.05	0.44508 ± 0.00134

a. Average tau from biexponential fit or single exponential fit. Error bars represent standard error of the mean from multiple cycles. Time resolution of spectroelectrochemistry is ≈ 10 ms.

b. Average tau from biexponential fit. We did not consider propagation time (t_p) here. Error bars represent standard error of the mean from multiple cycles. Time resolution of OECT is ≈ 10 µs.

c. Average tau from biexponential fit or single exponential fit. Error bars represent standard error of the mean from multiple cycles.

d. Tau from single exponential fit. Error bars represent standard error of the mean from multiple cycles.

Supplementary Table 4. Comparison of existing OECT transient models

Year Study	Operation Mode	Active Layer	Model	Delay Time	Asymmetric Switching
2007 Bernards et al[20]	Depletion	PEDOT:PSS	Empirical model based on RC charging circuit	No	No
2016 Gentile et al[21]	Depletion	PEDOT:PSS	Empirical model based on simple Randles equivalent circuit: R(R||C)	No	No
2017 Faria et al[22]	Depletion	PEDOT:PSS	Empirical model based on Randles equivalent circuit: R((RW)||C)	No	No
2017 Ersman et al[23]	Depletion	PEDOT:PSS	Empirical model based on custom equivalent circuit including p-type MOSFET	No	✓ - no physical explanation for asymmetric switching
2022 Paudel et al[24]	Depletion	PEDOT:PSS	2D drift–diffusion model	No	✓- (a) Model predicts τ_{off}/τ_{on} ratio (the asymmetry) depends strongly on drain potential (2 to 6 times), which is attributed to difference in vertical/lateral ionic current magnitude. Simulated results suggest τ_{off}/τ_{on} ratio weakly depends on thickness, ion mobility and channel length. (b) Experiment results show no systematic dependency of τ_{off}/τ_{on} ratio to drain/gate potential and channel thickness/length.
2023 Keene et al[25]	Depletion Accumulation	PEDOT:PSS p(g1T2-g5T2) p(g0T2-g6T2)	1D drift-diffusion model for depletion mode moving front experiment (primary comparisons are not for transistor geometries)	✓ - attribute to hole-limited propagating front	No
2023 This work	Accumulation	PB2T-TEG P3MEEMT P3HT	Empirical model based on direct operando microscopy observation	✓- attribute to ion-limited propagating front	✓– Model explains up to 500 times τ_{off}/τ_{on} ratio (switching asymmetry) observed in the experiment, which is attributed to a combination of (a) spatially heterogeneous doping and dedoping (front propagation) (b) asymmetric polymer doping/dedoping rate (due to differences in doping and dedoping kinetics) (c) amplification of the asymmetry due to non-linear response from the carrier-density-dependent mobility.

Supplementary Table 5. Comparison of doping front propagation speed of polymer-ion pairs in this study

Polymer	Ion	t_p (ms)	L (µm)	d (nm)[a]	v (µm /ms)[b]
PB2T-TEG	0.1 M KCl	~ 32	100	~ 50	~ 3.1
P3MEEMT	0.1M KCl	~ 88	100	~ 120	~ 1.1
P3MEEMT	0.1M KTFSI	~ 25	100	~ 120	~ 4.0
P3HT	0.1 M KTFSI	~ 80	100	~ 100	~ 1.3

a. Front propagation time is very sensitive to film thickness (d) as shown in **Supplementary Figure 12** and **Supplementary Figure 14**, suggesting that ion injection at the leading edge may play a role in front propagation speed.

b. Assume constant front propagation speed (v) as observed through operando microscopy.

Supplementary Notes

Supplementary Note 1. Transient fits with Bernards model

The Bernards model considers the transient behavior of an OECT as the characteristic of charging or discharging a capacitor.[20] Assuming charging or discharging occurs uniformly along the channel polymer, they proposed that I_D to have a single exponential response when switching between two steady-states:

$$I_D(t, V_G) = I_{ss}(V_G) + \Delta I_{ss}\left(1 - f\frac{\tau_e}{\tau_i}\right) \cdot e^{-t/\tau_i} \quad (1)$$

where I_{SS} is the steady-state channel current, and ΔI_{SS} is the current difference between two different steady-states. f determines the ratio of I_{GS} and I_{GD}. τ_e is the electronic charge transit time and τ_I is the product of $R_S \cdot C_{Ch}$. The R_S is the electrolyte resistance and the C_{Ch} is the channel capacitance.[20] They demonstrated the I_D response to be either a monotonic decay or a spike-and-recovery depending on the ratio between $f\tau_e$ and τ_I, with device switching speed determined by τ_i.[20]

As shown in **Fig 1a**, we found that Bernards model cannot accurately describe the transient response of accumulation mode OECTs. Most importantly, the Bernards model cannot explain the much faster device turn-off speed compared to turn-on phenomenon, which, based on the model, should be both equal to τ_I, as R_S and C_{Ch} are the same. We believe the reasons why Bernards model failed to predict the switching behavior of accumulation mode OECTs are as follows: first, the uniform charging or discharging assumption is inaccurate. Second, the carrier density dependent mobility needs to be considered, especially during device turn-off. Last, Bernards and Malliaras developed the model based on poly(3,4-ethylenedioxythiophene) doped with poly(styrene sulfonate) (PEDOT:PSS), which is a depletion mode OECT material.

Supplementary Note 2. Off-interval dependent OECT turn-on kinetics

Supplementary Figure 16 shows faster OECT turn-on kinetics through shortening the off-interval. To ensure the same electrochemical doping level is achieved, we fixed the on-interval to be 30 s for each cycle while varying the off-interval from 30 s to 1 s. Since the τ_{off} is much smaller than τ_{on} (see main text), the device could be turned off even with 1s off-interval in this case. It is clear that transistor turns on faster (smaller τ_{on}) with shorter off-interval. This phenomenon occurs because even though the transistor is at off-state already, dedoping of the channel polymer is not fully completed (see main text).

This behavior also implies that accumulation mode OECT turn-on kinetics is duty cycle dependent if the total period is carefully selected. Duty cycle is defined as the ratio between on-interval over the total period, and the total period is the sum of the on-interval and the off-interval. The duty-dependent kinetics may be beneficial for emulating neuron dynamic filtering function, in which the post synaptic response (i.e. I_D) depends on the duty of the presynaptic stimuli (i.e. V_G). Previously, Gkoupidenis et al.[26] and Yamamoto et al.[27] had demonstrated the dynamic filtering function with depletion mode, PEDOT:PSS-based OECTs. We note that asymmetry turn-on and turn-off period, or changing duty is not common for typical OECT transient characterization but may be useful for the aforementioned neuromorphic computing applications. We hope that our publication of these effects draws more attention to their discussion in the literature.

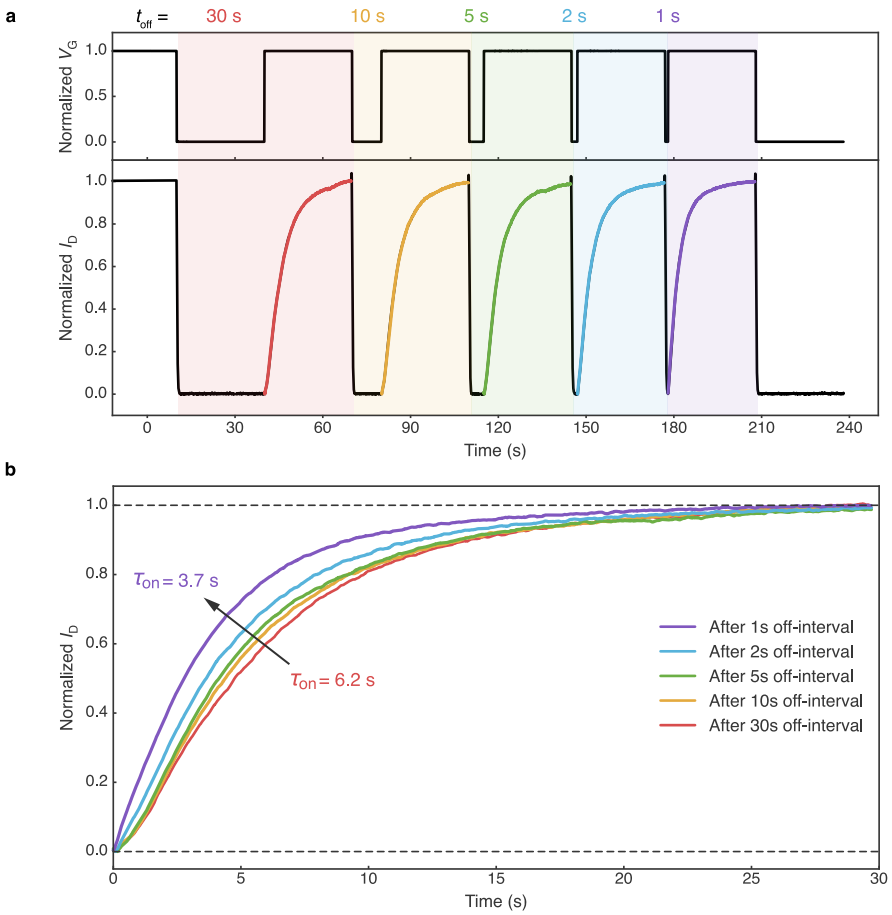

Supplementary Figure 16. Off-interval dependent OECT turn-on kinetics. (a) The transient response of a P3HT-based OECT with a fixed on-interval (30 s) and various off-intervals. Pre indicates previous runs for device stabilization. Numbers represent the cycle number. Transistor channel width, length and thickness is 4000 µm, 10 µm and ≈ 100 nm, respectively. (b) Comparison between turn-on kinetics with various off-intervals.

Supplementary Note 3. Carrier density-dependent mobility

Previously, with the exponentially distributed density of states (DOS) assumption, Friedlein et al. proposed the relation between OECT mobility and carrier concentration to be:

$$\mu = \mu_0 \cdot \left(\frac{p}{p_0}\right)^{\frac{E_0}{k_B T}-1} \quad (2)$$

where μ_0 is mobility prefactor and p_0 is zero-filed hole concentration. E_0 describes the energetic width of the tail of the density of states, k_B is Boltzmann's constant and T is temperature.[28] We found that our mobility and carrier concentration relation could be well characterized with this equation (**Fig. 4b** and **Supplementary Figure 17a**). The E_0 obtained from mobility and carrier concentration fit is ≈ 300 meV.

To justify our fitting result, we further estimated the E_0 value from the ultraviolet photoelectron spectroscopy (UPS) spectra data from our previous work.[29] **Supplementary Figure 17b** shows the estimation of E_0 value of PB2T-TEG via the exponential fit of the edge of HOMO region. We found the E_0 value is ≈ 204 meV, which we believe is close to the value obtained from mobility and carrier concentration fit, considering the difficulty to accurately determine the width of DOS via different techniques,[30,31] and the possible broadening of DOS after doping.[32] The similar E_0 values obtained by two different methods verify that our approach studying mobility and carrier density relation is feasible.

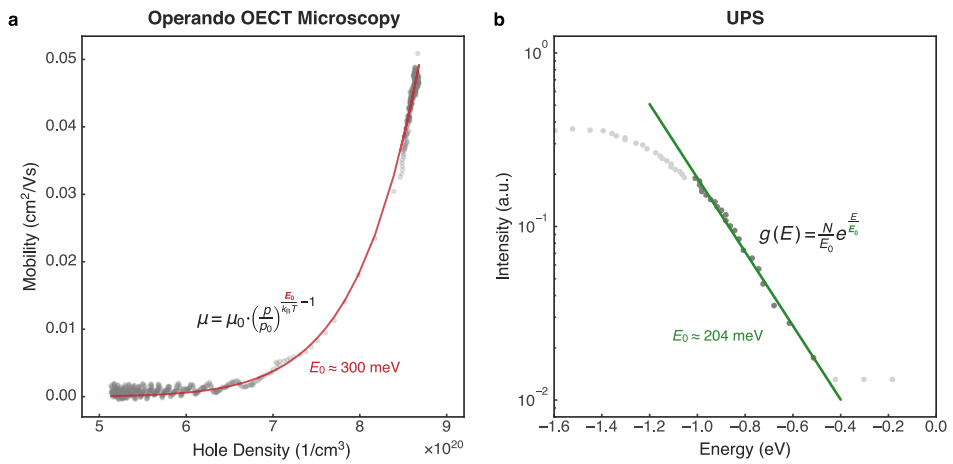

Supplementary Figure 17. The estimation of the energetic width of the tail of the density of states (E_0) with (a) OECT mobility and concentration fit and (b) via ultraviolet photoelectron spectroscopy (UPS). N represents number of states, E is the energy, and g is the DOS in the equation in (b).

Supplementary Note 4. The impact of E_0 to asymmetric OECT turn-on and turn-off kinetics

To study the impact of E_0 to OECT turn-on and turn-off kinetics, we first derived a $I_D(t)$ model starting from the relation between carrier density and time, $p(t)$, which is directly measured from optical microscopy experiment as shown in the top panel of **Supplementary Figure 18**. We note that during the doping front propagation stage, the dark green line and light green line represent the carrier density of the doped and undoped (or dedoped) region, respectively. Using the mobility-density (μ-p) equation (Equation 2 or Equation S2), we could then calculate the relation between carrier mobility and time, $\mu(t)$, which is shown in the middle panel of **Supplementary Figure 18**. Last, using the Ohm's law, the relation between drain current and time, $I_D(t)$, could be expressed as $V_D/R_{channel}(t)$, as shown in the bottom panel of **Supplementary Figure 18**. We found the as derived $I_D(t)$ model could largely reproduce the behavior of actual measured $I_D(t)$ data, especially the initial stage of the turn-on and the turn-off.

The relation between transistor channel resistance, $R_{channel}(t)$ could be expressed as:

$$R_{\text{channel}}(t) = \begin{cases} \dfrac{\mathrm{L}}{W \cdot d \cdot e} \cdot \left[\dfrac{1}{\mu_d(t) \cdot p_d(t)} \cdot \dfrac{t}{t_p} + \dfrac{1}{\mu_u(t) \cdot p_u(t)} \cdot \left(1 - \dfrac{t}{t_p}\right) \right] & \left(\text{doping front propagation, } t < t_p\right) \quad (3) \\ \dfrac{\mathrm{L}}{W \cdot d \cdot e} \cdot \dfrac{1}{\mu(t) \cdot p(t)} & \text{(vertical doping and dedoping)} \quad (4) \end{cases}$$

where L, W, and d represent channel length, width, and thickness, respectively. t is time, t_p is the propagation time and e is the electron charge. μ_d and μ_u represent the carrier mobility in the doped region and undoped region during the front propagation stage. p_d and p_u represent the carrier (hole) density in the doped region and undoped region during the front propagation stage. μ and p represent the averaged hole carrier mobility and carrier density during vertical doping and dedoping stage.

The $R_{channel}(t)$ during doping front propagation at time point t where $t < t_p$ could be expressed as the two resistors (R_{doped} and $R_{undoped}$) connected in series:

$$R_{channel}(t)$$

$$= R_{doped}(t) + R_{undoped}(t)$$

$$= \rho_d \cdot \frac{L_d(t)}{W \cdot d} + \rho_u \cdot \frac{L_u(t)}{W \cdot d}$$

$$= \rho_d \cdot \frac{v \cdot t}{W \cdot d} + \rho_u \cdot \frac{(L - v \cdot t)}{W \cdot d}$$ (constant front propagating speed (v) as observed in experiments)

$$= \frac{1}{\sigma_d} \cdot \frac{\frac{L}{t_p} \cdot t}{W \cdot d} + \frac{1}{\sigma_u} \cdot \frac{\left(L - \frac{L}{t_p} \cdot t\right)}{W \cdot d} \qquad \left(v = \frac{L}{t_p}\right)$$

$$= \frac{1}{\mu_d \cdot p_d \cdot e} \cdot \frac{\frac{L}{t_p} \cdot t}{W \cdot d} + \frac{1}{\mu_u \cdot p_u \cdot e} \cdot \frac{\left(L - \frac{L}{t_p} \cdot t\right)}{W \cdot d}$$

$$= \frac{\mathrm{L}}{W \cdot d \cdot e} \cdot \left[\frac{1}{\mu_d(t) \cdot p_d(t)} \cdot \frac{t}{t_p} + \frac{1}{\mu_u(t) \cdot p_u(t)} \cdot \left(1 - \frac{t}{t_p}\right)\right]$$

$$\approx \frac{\mathrm{L}}{W \cdot d \cdot e} \cdot \left[\frac{1}{\mu_u(t) \cdot p_u(t)} \cdot \left(1 - \frac{t}{t_p}\right)\right] \qquad \text{as } \mu_u(t) \cdot p_u(t) \ll \mu_d(t) \cdot p_d(t) \text{ for } t < t_p$$

where L_d is length of the doped region, L_u is the length of the undoped region ($L = L_u + L_d$), v is the doping front propagation speed. ρ_d and $\rho_u$represent the resistivity of the doped and undoped region. σ_d and σ_u represent the conductivity of the doped and undoped region. Because $\mu_u(t) \cdot p_u(t) \ll \mu_d(t) \cdot p_d(t)$, the R_{undoped} dominates the R_{channel} during the front propagation stage.

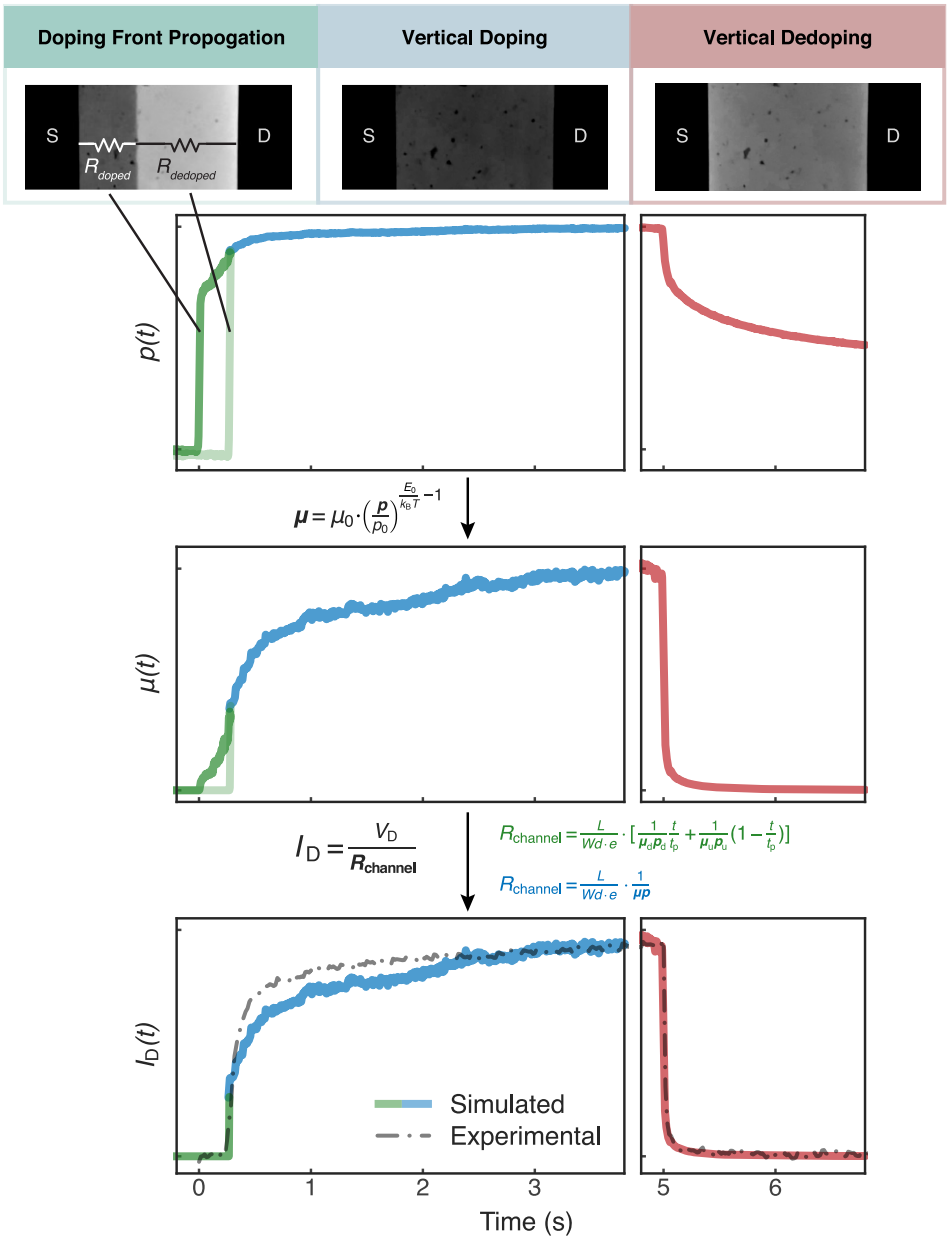

Supplementary Figure 18. The relation between I_D and time (experimental data and the simulated model). The top panel shows the relation between carrier density (p) and time measured from the optical microscopy experiment. We note that during the doping front propagation stage, the dark green line and light green line represents the carrier density of the doped and undoped (or dedoped) region, respectively. The relation between carrier mobility (μ) and time (the middle panel) is derived from $p(t)$ relation via the μ-p equation (Equation 2 or Equation S2). From Ohm's law, the simulated $I_D(t)$ could then be expressed as $V_D/R_{channel}(t)$ (the bottom panel). The $R_{channel}$ (t) is shown in the Equation S3 and Equation S4. Note that during the front propagation stage, the resistance in the undoped region, $R_{undoped}$ dominates the channel resistance, $R_{channel}$ such that the I_D remains relatively low even with increased carrier density and carrier mobility in the doped region. We found the as derived $I_D(t)$ model could largely reproduce the behavior of actual measured $I_D(t)$ data, especially in the initial stage of the turn-on and the turn-off.

Supplementary Figure 19 shows the impact of E_0 values to the asymmetry of OECT turn-on and turn-off kinetics. The top panel of **Supplementary Figure 19** shows the relation between carrier density and time, $p(t)$ measured from optical microscopy experiment. Using the μ-p equation (Equation 2 or Equation S2), we then simulated the $\mu(t)$ as well as $I_D(t)$ with various E_0 values, which are shown in the middle and the bottom panel of **Supplementary Figure 19**. We found that as the E_0 values decreased, the turn-on time decreases while the turn-off time increases, resulting in the reduced asymmetry between turn-on and turn-off time. This result suggests that, to reduce the OECT turn-on and turn-off time difference, one should seek materials with higher crystallinity (smaller E_0). We note that however, the relation between polymer film crystallinity and OECT performance could be very complex. Higher crystallinity may have negative impacts on ionic carrier uptake[33] and electronic carrier transport.[34]

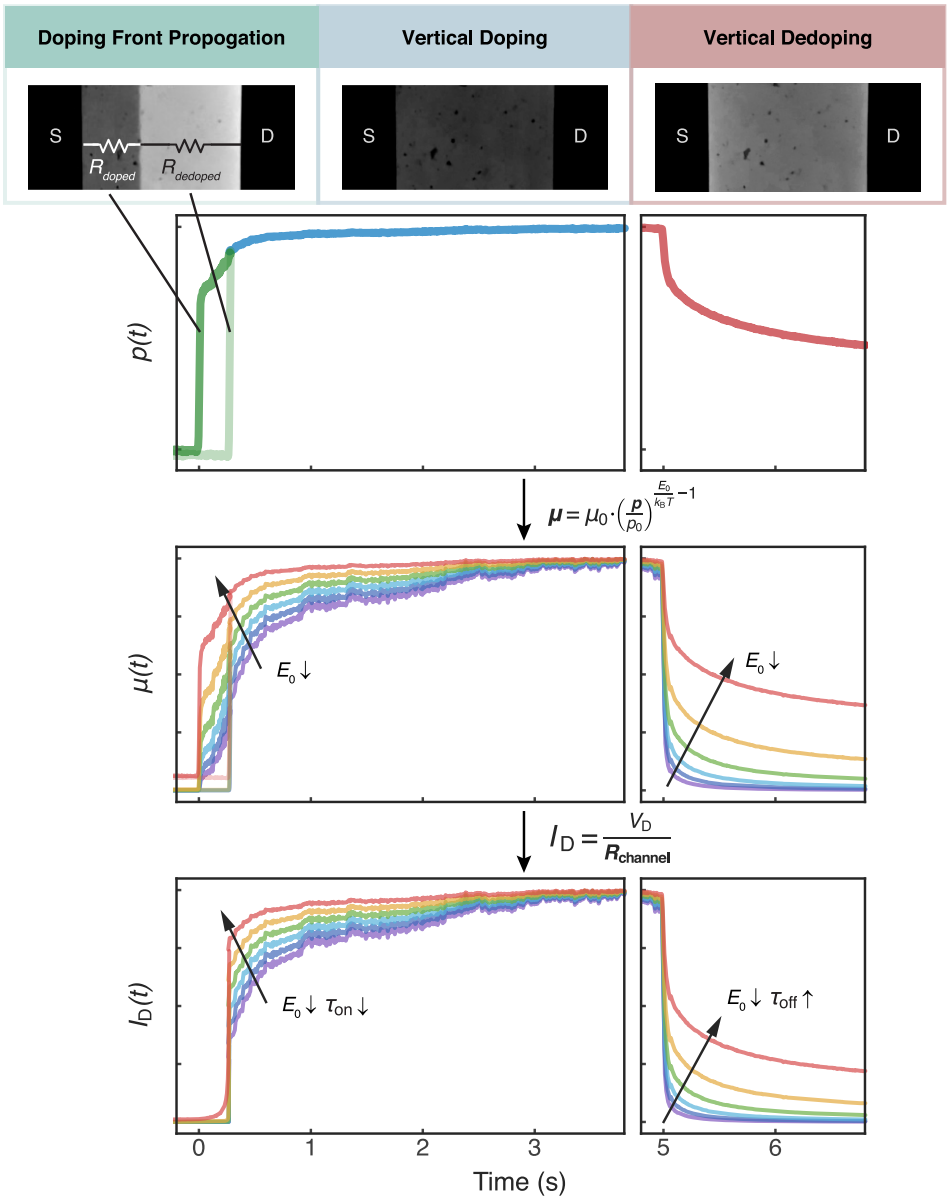

Supplementary Figure 19. The impact of E_0 to asymmetric OECT turn-on and turn-off kinetics. The top panel shows the relation between carrier density (p) and time, $p(t)$ measured from the optical microscopy experiment. We note that during the doping front propagation stage, the dark green line and light green line represents the carrier density of the doped and undoped (or dedoped) region, respectively. The relation between carrier mobility (μ) and time (the middle panel) is derived from $p(t)$ relation via the μ-p equation (Equation 2 or Equation S2) with various E_0 values arbitrarily given. From Ohm's law, the simulated $I_D(t)$ could then be expressed as $V_D/R_{channel}(t)$ (the bottom panel). The $R_{channel}(t)$ is shown in the Equation S3 and Equation S4. We found that as the E_0 values decreased, the turn-on time decreases while the turn-off time increases, resulting in the reduced asymmetry between turn-on and turn-off time.

Supplementary Note 5. SPICE simulation

Here, we attempt to replicate the delayed turn-on (doping front propagation stage) and asymmetric kinetics via circuit modeling. To the best of our knowledge, Ersman et al. are the only ones to report an OECT circuit model including active elements and show asymmetric kinetics with depletion mode OECTs.[23] In their approach, a diode was used to represent the discharging path from the body of a SPICE MOSFET model. Though their model can indeed represent asymmetric kinetics, it does not intuitively capture the physics of an OECT, because unlike a MOSFET, there is no body terminal in an OECT. On the other hand, purely passive element circuit models are very popular, as in those developed by Bernards et al. and Faria et al. that have seen widespread adoption.[20,22] However, such circuit models are linear and thus cannot exhibit different turn-on and turn-off kinetics. For details, the reader is referred to reviews on circuit model kinetics,[35–37] and a more systematic modeling is beyond the scope of this manuscript.

To reconcile these two approaches with our experimental data, based on the classical $R_s+(R_{ct}||C_p)$ model commonly used in literature,[22,38] we include a time-dependent resistance to represent the channel polymer resistivity; this reflects the resistor component discussed in **Supplementary Note 4** above. The RC component could reflect the initial "spike" in both I_G and I_D, while the time-dependent resistance could replicate the timing. **Supplementary Figure 20a** shows the proposed equivalent circuit model. Here, V_G is the gate potential and V_D is the drain potential. R_s is the solution resistance, $R_D(t)$ is the time-dependent resistance and R_{ss} is the source electrode contact used for measuring current in SPICE simulation. C_p and R_{ct} are the polymer volume capacitance and charge transfer resistance commonly applied in Randles circuit. R_s, C_p, R_{ct} have limited effects on the kinetics through the channel in this proposed model, where they represent the electrolyte-drain interface, rather than the entire active layer. We also included a constant current source to represent the gate leakage current, $f \times I_G$, which does not affect the kinetics here. The detailed explanation of f factor could be found in Faria and Bernards models.[20,22]

Supplementary Figure 20b shows the transient response and SPICE simulation result of an example accumulation mode P3HT OECT operating 0.1 M KTFSI. ($W/L/d$ = 5 mm/100 μm/100 nm) The drain potential is fixed at −0.6 V while the on-potential is −0.2 V and off-potential is −0.6 V. We modeled the time-dependent

resistance $R_D(t)$ by an exponential decay from a high resistance (undoped) state to a low resistance state (doped) or vice versa:

$$R_D(t) = \begin{cases} V_D/I_{D,sat} + C\left(1 - e^{-\frac{t}{\tau_{off}}}\right) & \text{(turn-off)} \\ V_D/I_{D,sat} + Ae^{-\frac{t}{\tau_1}} + Be^{-\frac{t}{\tau_2}} & \text{(turn-on)} \end{cases}$$

where A, B, and C are constants. $I_{D,sat}$ is the expected saturation current, or the on-state current. τ_1, τ_2, and τ_{off} are the time constants associated with the transistor turn-on stage (which has two components as discussed in the main text), and the transistor turn-off stage. We demonstrated that the SPICE model could accurately reflect the transient asymmetry, with the time constants τ_1, τ_2, and τ_{off} being 0.7 s, 2 s, and 0.5 s, consistent with observations of faster device turn-off behavior. We also note that the parameters used for fitting here including solution resistance ($R_s \approx$ 1 kΩ), polymer volume capacitance ($C_p \approx 2.4$ μF) and charge transfer resistance ($R_{ct} \approx 10$ kΩ) are all close to the actual physical values, verifying the proposed model captures the physics of OECT switching. Constants related to time-dependent resistance, namely, A, B and C all have values around 1000 in this specific example. We expect these values to vary with different polymers and channel geometry. All SPICE simulations were performed with LTSpice (freely available from Analog Devices).

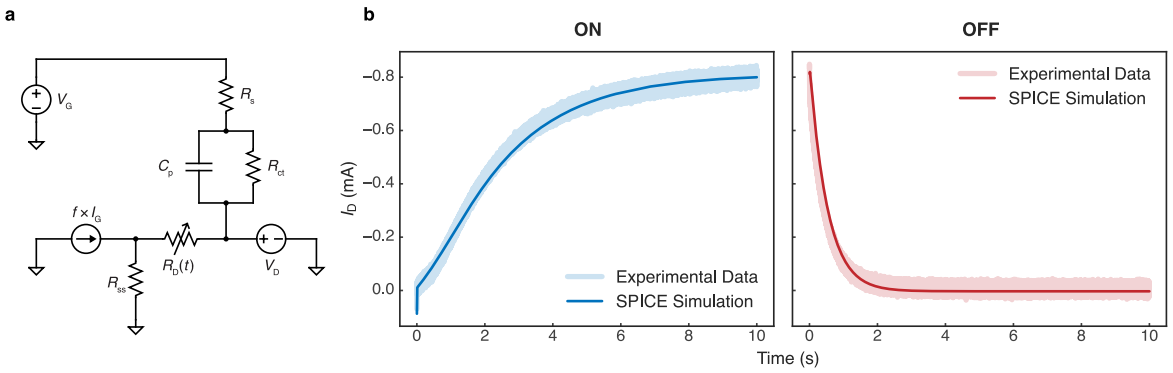

Supplementary Figure 20. SPICE simulation of an accumulation mode OECT. **a**, LTSpice circuit model. Here, we used $f = 0.5$, though in this work the nature of f parameter is not under investigation. R_{ss} is used only for simulation purposes to measure the total source current, and it is generally a trivially low resistance (0.01 Ω). The other values are defined in the discussion above. **b**, Experimental data of an example accumulation mode P3HT OECT operates in 0.1 M KTFSI and the SPICE simulation results. ($W/L/d$ = 5 mm/100 μm/100 nm) The drain potential is fixed at −0.6 V while the on-potential is −0.6 V and off-potential is −0.2 V. We showed that the turn-on and turn-off kinetics are well represented by the circuit.

Supplementary Note 6. Other design factors for fast OECTs

Besides the operation variables studied in this work (operation potentials, ion concentrations, ion species and channel dimensions), other factors including the size and the type of gate electrode, gate-channel distance, and parasitic capacitance may also be crucial when designing fast OECTs, especially for transistors with even smaller dimensions (sub μm to nm scale). We briefly discuss how these factors may affect kinetics below.

Common choices of OECT gate electrodes are non-polarizable gate (i.e., Ag/AgCl pellet) and polarizable gate (i.e., gold or platinum). For a non-polarizable gate, the voltage drop at the gate/electrolyte interface is negligible as the gating is through Faradaic reactions.[39] For a polarizable gate, the gate capacitance (proportional to gate area) is typically more than ten times larger than channel capacitance for effective gating due to the potential drop at the gate/electrolyte interface.[39] A common strategy to increase the gate capacitance is to use a thick PEDOT:PSS layer as the gate electrode.[40] We note that, to our best of knowledge, OECT operation speed difference between Ag/AgCl pellet, gold gate and PEDOT:PSS gate has not yet been systematically studied, partly due to the difficulty to control the doping level to be the same with different gate electrodes. In our present study, we studied the OECT transient behavior using Ag/AgCl pellet as gate electrode, which is the most commonly used OECT gate electrode to date.

The other factor to consider when designing fast OECTs is the gate-channel distance. Qualitatively, shorter gate-channel distance is preferred for faster OECT response as the solution resistance decreased with smaller gate-channel distance.[20] Quantitively, the exact impact of gate-channel distance to the OECT operation speed has not yet been thoroughly investigated, likely because the common Ag/AgCl gate pellet is typically dangling in the solution, and the exact gate-channel distance is thus difficult to control/defined and less reported. In our present study, we maintained a consistent gate-channel distance of approximately 5 mm, aligned with the height of the electrolyte chamber. We believe 5 mm gate-channel distance is a reasonably small distance for Ag/AgCl pellet to not be in direct contact with the channel and to effectively gate the channel. To further reduce the channel-gate distance, one may need to use lithography technique and adopt planar gate design.

Lastly, parasitic capacitance, or electric double layer (EDL) capacitor formed between source/electrolyte and drain/electrolyte, could also affect the transistor switching speed. Bidoky et al had demonstrated that the operating frequency of P3HT-based electrolyte-gated organic filed-effect transistors (EG-OFETs) could be increased by 10-fold if the parasitic capacitance is reduced through minimizing the contact area between the electrolyte and the source and drain electrodes.[41] In general, minimizing the contact area between the electrolyte and the source and drain electrodes (small parasitic capacitance) is desired for both EG-OFETs and OECTs, which could be accomplished by covering the top surface of the source and drain electrodes with insulating, low dielectric materials like Parylene C.[42]

Supplementary Note 7. Comparison of existing OECT transient models

Supplementary Table 4 shows the summary comparison of existing OECT transient models. Early models based on equivalent circuit with only passive elements (resistance and capacitance) could describe the turn-off behavior (gate potential applied) of PEDOT:PSS based OECTs but fail to predict the asymmetric OECT switching rates.[20–22] With custom equivalent circuit including an active element (p-MOSFET), Ersman et al. attempted to replicate asymmetric switching behavior of PEDOT:PSS based OECTs, though the exact function of the elements or circuit topology are not ascribed to physical processes.[23] Recently, Paudel et al. demonstrated a first rigorous 2D drift-diffusion OECT model for PEDOT:PSS based depletion mode OECTs.[24] Their quantitative physical model predicts τ_{off}/τ_{on} ratio (the asymmetry) depends strongly on drain potential (2 to 6 times) (Fig 13b),[24] which is attributed to difference in vertical/lateral ionic current magnitude (Fig 6),[24] as opposed to disorder in the polymer itself (carrier density-dependent mobility is missing). In addition, their simulated results show τ_{off}/τ_{on} ratio (the asymmetry) is weakly dependent on thickness, ion mobility and channel length (Fig 9).[24] Nevertheless, their experiment results show no systematic dependency of τ_{off}/τ_{on} ratio to drain/gate potential and channel thickness/length (Fig 10, Fig 12 and Fig14).[24] We thus propose that vertical/lateral ionic current predicted by their model *alone* cannot explain the magnitude of the asymmetry results encountered in real accumulation mode OECTs as shown in this work even if the operating parameters (i.e., drain potential, thickness, ion mobility and channel length) are taken to extremes (e.g., negative film thicknesses).

In terms of hole transport in the polymer, Keene et al. very recently investigated the electrochemical doping behavior of both PEDOT:PSS and p(g1T2-g5T2) via optical moving front experiments, predominantly in 2-terminal configurations.[25] They conclude that the hole-limited doping leads to a delay during the turn-on of p(g1T2-g5T2) based accumulation mode OECTs.[25] Even though both the exciting work by Keene et al. [25] and this study show that the turn-on delay state is due to doping front propagation, our work provides unique new insight to the transient asymmetry of accumulation mode OECTs, and we interpret our experimental data as indicating that the propagating front, in an OECT at least, must be interpreted in the context of ionic processes. For instance, the front propagation speed is 4 times faster with KTFSI compared to KCl for the same polymer as shown in **Supplementary Table 5**.

To this end, our data show that the doping front speed depends on ion type, ion concentration, and gate voltage, but is independent of source-drain potential (**Fig. 5**). Because the source-drain potential would affect the drift velocity of holes in the channel, we would expect the doping front speed to change with source-drain potential if it were primarily dominated by hole mobility.

Turning back to the asymmetry in switching times, we believe this asymmetry, which can be as large as 500 times difference (2 orders of magnitude larger than predicted by Paudel et al.'s simulation work[24]), originates in part from the structural/reorganizational differences between polymer doping and dedoping processes. These differences are captured in the asymmetric 2-terminal spectroelectrochemical bleaching rates. *However, a critical insight here is that this asymmetry is accentuated in non-linear fashion by the (density of states-dependent) carrier-density-dependence of the hole mobility, given that the asymmetry of the transistor switching speeds is always much larger than the asymmetry of the doping/dedoping rates measured by spectroelectrochemistry.* Since the carrier-density-dependent mobility depends on disorder, our model shows how a material-dependent parameter (disorder) can help explain the asymmetry that is missing from the Paudel model, while the experimental observation of effect of ion types on *transistor* asymmetry provides critical benchmarks to test existing and future models.

Supplementary Note 8. Limitations of our proposed model

The model we propose in this work captures the switching behavior of accumulation mode OECTs, reproduces the carrier-density mobility of the organic semiconductor, and it even fits with physically meaningful density of states. Nevertheless, our model has limitations, most notably in its empirical nature. We must include observational biexponential/exponential models to describe the experimental data. Nevertheless, when we do so, we obtain carrier-density-dependent mobilities that follow the forms long-used to describe such behaviors in organic semiconductors, while at the same time generating reasonable estimates of the density of states in the polymer. In the future, we hope that a first principles drift-diffusion simulation that fully incorporates polymer microstructure, chemical interactions with different ions, and includes the polymer density of states, that could be used to develop a universal OECT transient model that explicitly describes the relation between OECT switching times and operation variables (V_D, V_G, W, d, L, C_{ion}) and ultimately the kinetics OECT material figure of merit, similar to the steady-state material figure of merit (μC^*) identified by Inal et al.[43] With such a universal OECT transient model, one will be able to predict OECT turn-on and turn-off time with selected operation variables once the electrochemical doping and dedoping speed of the polymer (intrinsic material property) is known (i.e., via spectroelectrochemistry). Additionally, numerical simulation for accumulation mode OECT transient response has not yet been accomplished. We expect the 2D drift–diffusion models for accumulation mode OECTs based on the foundations laid by Paudel et al.[24] and Keene et al.[25] will help to further elucidate the complex OECT switching behavior, with a particular emphasis on asymmetry, the role of different ion chemistries, and the effects of polymer disorder/density of states.

References

1. Huang, W. *et al.* Vertical organic electrochemical transistors for complementary circuits. *Nature* **613**, 496–502 (2023).

2. Giovannitti, A. *et al.* Controlling the mode of operation of organic transistors through side-chain engineering. *Proc. Natl. Acad. Sci. U. S. A.* **113**, 12017–12022 (2016).

3. Li, P., Shi, J., Lei, Y., Huang, Z. & Lei, T. Switching p-type to high-performance n-type organic electrochemical transistors via doped state engineering. *Nat. Commun.* **13**, 5970 (2022).

4. Jia, H. *et al.* Engineering donor-acceptor conjugated polymers for high-performance and fast-response organic electrochemical transistors. *J. Mater. Chem. C* **9**, 4927–4934 (2021).

5. Giovannitti, A. *et al.* Energetic Control of Redox-Active Polymers toward Safe Organic Bioelectronic Materials. *Adv. Mater.* **32**, 1908047 (2020).

6. Wu, X. *et al.* All-Polymer Bulk-Heterojunction Organic Electrochemical Transistors with Balanced Ionic and Electronic Transport. *Adv. Mater.* **34**, 2206118 (2022).

7. Wang, Y. *et al.* The effect of the donor moiety of DPP based polymers on the performance of organic electrochemical transistors. *J. Mater. Chem. C* **9**, 13338–13346 (2021).

8. Luo, X. *et al.* Designing Donor–Acceptor Copolymers for Stable and High-Performance Organic Electrochemical Transistors. *ACS Macro Lett.* **10**, 1061–1067 (2021).

9. Chen, S. E. *et al.* Impact of varying side chain structure on organic electrochemical transistor performance: a series of oligoethylene glycol-substituted polythiophenes †. *J. Mater. Chem. A* **10**, 10738–10749 (2022).

10. Wang, Y. *et al.* Hybrid Alkyl-Ethylene Glycol Side Chains Enhance Substrate Adhesion and Operational Stability in Accumulation Mode Organic Electrochemical Transistors. *Chem. Mater.* **31**, 9797–9806 (2019).

11. Giridharagopal, R., Guo, J., Kong, J. & Ginger, D. S. Nanowire Architectures Improve Ion Uptake Kinetics in Conjugated Polymer Electrochemical Transistors. *ACS Appl. Mater. Interfaces* **13**, 34616–34624 (2021).

12. Wu, H. Y. *et al.* Influence of Molecular Weight on the Organic Electrochemical Transistor Performance of Ladder-Type Conjugated Polymers. *Adv. Mater.* **34**, 2106235 (2022).

13. Chen, J. *et al.* Backbone coplanarity manipulation via hydrogen bonding to boost the n-type performance of polymeric mixed conductors operating in aqueous electrolyte. *Mater. Horizons* **10**, 607–618 (2023).

14. Shi, J. *et al.* Revealing the Role of Polaron Distribution on the Performance of n-Type Organic Electrochemical Transistors. *Chem. Mater.* **34**, 864–872 (2022).

15. Feng, K. *et al.* Cyano-Functionalized n-Type Polymer with High Electron Mobility for High-Performance Organic Electrochemical Transistors. *Adv. Mater.* **34**, 2201340 (2022).

16. Wang, Y. *et al.* n-Type Organic Electrochemical Transistors with High Transconductance and Stability. *Chem. Mater.* **35**, 405–415 (2022).

17. Guo, J. *et al.* Hydration of a Side-Chain-Free n-Type Semiconducting Ladder Polymer Driven by Electrochemical Doping. *J. Am. Chem. Soc.* **145**, 1866–1876 (2023).

18. Feng, K. *et al.* Fused Bithiophene Imide Dimer-Based n-Type Polymers for High-Performance Organic Electrochemical Transistors. *Angew. Chemie Int. Ed.* **60**, 24198–24205 (2021).

19. Sun, H. *et al.* Complementary Logic Circuits Based on High-Performance n-Type Organic Electrochemical Transistors. *Adv. Mater.* **30**, 1704916 (2018).

20. Bernards, D. A. & Malliaras, G. G. Steady-state and transient behavior of organic electrochemical transistors. *Adv. Funct. Mater.* **17**, 3538–3544 (2007).

21. Gentile, F. *et al.* A theoretical model for the time varying current in organic electrochemical transistors in a dynamic regime. *Org. Electron.* **35**, 59–64 (2016).

22. Faria, G. C., Duong, D. T. & Salleo, A. On the transient response of organic electrochemical transistors. *Org. Electron.* **45**, 215–221 (2017).

23. Ersman, P. A. *et al.* Screen printed digital circuits based on vertical organic electrochemical transistors. *Flex. Print. Electron.* **2**, 045008 (2017).

24. Paudel, P. R. *et al.* The Transient Response of Organic Electrochemical Transistors. *Adv. Theory Simul.* 2100563 (2022).

25. Keene, S. T. *et al.* Hole-limited electrochemical doping in conjugated polymers. *Nat. Mater.* **22**, 1121–1127 (2023).

26. Gkoupidenis, P., Schaefer, N., Garlan, B. & Malliaras, G. G. Neuromorphic Functions in PEDOT:PSS Organic Electrochemical Transistors. *Adv. Mater.* **27**, 7176–7180 (2015).

27. Yamamoto, S. & Malliaras, G. G. Controlling the Neuromorphic Behavior of Organic Electrochemical Transistors by Blending Mixed and Ion Conductors. *ACS Appl. Electron. Mater.* **2**, 2224−2228 (2020).

28. Friedlein, J. T., Shaheen, S. E., Malliaras, G. G. & McLeod, R. R. Optical Measurements Revealing Nonuniform Hole Mobility in Organic Electrochemical Transistors. *Adv. Electron. Mater.* **1**, 1500189 (2015).

29. Zhang, Z. *et al.* Modulate Molecular Interaction between Hole Extraction Polymers and Lead Ions toward Hysteresis-Free and Efficient Perovskite Solar Cells. *Adv. Mater. Interfaces* **5**, 1800090 (2018).

30. Nakano, K., Kaji, Y. & Tajima, K. Highly Sensitive Evaluation of Density of States in Molecular Semiconductors by Photoelectron Yield Spectroscopy in Air. *ACS Appl. Mater. Interfaces* **13**, 28574–28582 (2021).

31. Bässler, H., Kroh, D., Schauer, F., Nádaždy, V. & Köhler, A. Mapping the Density of States Distribution of Organic Semiconductors by Employing Energy Resolved–Electrochemical Impedance Spectroscopy. *Adv. Funct. Mater.* **31**, 2007738 (2021).

32. Hase, H., Berteau-Rainville, M., Charoughchi, S., Orgiu, E. & Salzmann, I. Doping-related broadening of the density of states governs integer-charge transfer in P3HT. *Appl. Phys. Lett.* **118**, 203301 (2021).

33. Giridharagopal, R. *et al.* Electrochemical strain microscopy probes morphology-induced variations in ion uptake and performance in organic electrochemical transistors. *Nat. Mater.* **16**, 737–742 (2017).

34. Flagg, L. Q. *et al.* Polymer Crystallinity Controls Water Uptake in Glycol Side-Chain Polymer Organic Electrochemical Transistors. *J. Am. Chem. Soc.* **141**, 4345–4354 (2019).

35. Colucci, R., Barbosa, H. F. D. P., Günther, F., Cavassin, P. & Faria, G. C. Recent advances in modeling organic electrochemical transistors. *Flex. Print. Electron.* **5**, 013001 (2020).

36. Friedlein, J. T., McLeod, R. R. & Rivnay, J. Device physics of organic electrochemical transistors. *Org. Electron.* **63**, 398–414 (2018).

37. Paudel, P. R., Tropp, J., Kaphle, V., Azoulay, J. D. & Lüssem, B. Organic electrochemical transistors-from device models to a targeted design of materials. *J. Mater. Chem. C* **9**, 9761–9790 (2021).

38. Lago, N. *et al.* A physical-based equivalent circuit model for an organic/electrolyte interface. *Org. Electron.* **35**, 176–185 (2016).

39. Rivnay, J. *et al.* Organic electrochemical transistors. *Nat. Rev. Mater.* **3**, 17086 (2018).

40. Koutsouras, D. A., Torricelli, F., Gkoupidenis, P. & Blom, P. W. M. Efficient Gating of Organic Electrochemical Transistors with In-Plane Gate Electrodes. *Adv. Mater. Technol.* **6**, 2100732 (2021).

41. Zare Bidoky, F., Hyun, W. J., Song, D. & Frisbie, C. D. Printed, 1 V electrolyte-gated transistors based on poly(3-hexylthiophene) operating at >10 kHz on plastic. *Appl. Phys. Lett.* **113**, 53301 (2018).

42. Ohayon, D., Druet, V. &Inal, S. A guide for the characterization of organic electrochemical transistors and channel materials. *Chem. Soc. Rev.* 1001–1023 (2023).

43. Inal, S., Malliaras, G. G. & Rivnay, J. Benchmarking organic mixed conductors for transistors. *Nat. Commun.* **8**, 1767 (2017).